LCP NANOPARTICLE FOR TUMOR AND LYMPH NODE METASTASIS IMAGING

Yu-Cheng Tseng

A dissertation submitted to the faculty of the University of North Carolina at Chapel Hill in partial fulfillment of the requirements for the degree of Doctorate of Philosophy in the Department of Molecular Pharmaceutics, Eshelman School of Pharmacy.

Chapel Hill
2013

Approved by:

Leaf Huang, Ph.D.

Xiao Xiao, Ph.D.

Michael Jay, Ph.D.

Wenbin Lin, Ph.D.

Weili Lin, Ph.D.

ABSTRACT

YU-CHENG TSENG: LCP Nanoparticle for Tumor and Lymph Node Metastasis Imaging
(Under the direction of Dr. Leaf Huang)

A lipid/calcium/phosphate (LCP) nanoparticle formulation (particle diameter ~25 nm) has previously been developed to delivery siRNA with superior efficiency. In this work, ^{111}In was formulated into LCP nanoparticles to form ^{111}In-LCP for SPECT/CT imaging. With necessary modifications and improvements of the LCP core-washing and surface-coating methods, ^{111}In-LCP grafted with polyethylene glycol exhibited reduced uptake by the mononuclear phagocytic system. SPECT/CT imaging supported performed biodistribution studies, showing clear tumor images with accumulation of 8% or higher injected dose per gram tissue (ID/g) in subcutaneous, human-H460, lung-cancer xenograft and mouse-4T1, breast cancer metastasis models. Both the liver and the spleen accumulated ~20% ID/g. Accumulation in the tumor was limited by the enhanced permeation and retention effect and was independent of the presence of a targeting ligand. A surprisingly high accumulation in the lymph nodes (~70% ID/g) was observed. In the 4T1 lymph node metastasis model, the capability of intravenously injected ^{111}In-LCP to visualize the size-enlarged and tumor-loaded sentinel lymph node was demonstrated. By analyzing the SPECT/CT images taken at different time points, the PK profiles of ^{111}In-LCP in the blood and major organs were determined. The results indicated that the decrement of ^{111}In-LCP blood concentration was not due to excretion, but to tissue penetration, leading to lymphatic accumulation.

Larger LCP (diameter ~65 nm) nanoparticles were also prepared for the purpose of comparison. Results indicated that larger LCP achieved slightly lower accumulation in the tumor and lymph nodes, but much higher accumulation in the liver and spleen; thus, larger nanoparticles might not be favorable for imaging purposes. We also demonstrated that LCP with a diameter of ~25 nm were better able to penetrate into tissues, travel in the lymphatic system and preferentially accumulate in the lymph nodes due to 1) small size, 2) a well-PEGylated lipid surface, and 3) a slightly negative surface charge. The ability of ~25 nm LCP to deliver genes to the lymph nodes via IV injection was illustrated by RFP cDNA expression. The results promise the potential use of LCP nanoparticles as formulations for the multifunctional, systemic delivery of both imaging and therapeutic agents to both tumors and lymph nodes.

ACKNOWLEDGEMENTS

Completion of this thesis would not have been possible without the help of many people. First, I would like to thank my dissertation mentor, Professor Leaf Huang, for a great deal of support throughout my graduate career and teaching me the skills necessary to become an independent scientist. He created a scientific environment that encouraged novel ideas and provided the resources and great insights to help students pursue them. I would also like to thank the members of my committee, Professor Xiao Xiao, Professor Michael Jay, Professor Wenbin Lin, Professor Weili Lin, and Professor Leaf Huang, for their support and intellectual contributions to this work. Their comments and suggestions were incredibly helpful. Also, I enjoy the help and scientific discussion I had with many of the Huang lab members. I'd also like to express my appreciations to my family and girlfriend for their companionship during and great support toward my PhD study overseas. I feel truly grateful to God for leading me here to UNC and bringing all of these great people to my life. It's been such a blessing to be here, I will miss this place.

TABLE OF CONTENTS

LIST OF TABLES

LIST OF FIGURES

LIST OF ABBREVIATIONS AND SYMBOLS

^{111}In	Indium-111
CaP	Calcium-Phosphate
CT	Computed tomography
DLS	Dynamic light scattering
DOPA	Dioleoylphosphatydic acid
DOPC	Dioleoylphosphatidylcholine
DOTA	1,4,7,10-tetraazacyclododecane-1,4,7,10-tetraacetic acid
DOTAP	1,2-dioleoyl-3-trimethylammonium-propane
DSPE-PEG_{2000}	1,2-distearoyl-sn-glycero-3-phosphoethanolamine-N-poly(ethylene glycol)2000
DTPA	Diethylene triamine pentaacetic acid
EPR effect	Enhanced permeation and retention effect
ER	Endoplasmic reticulum
EtOH	Ethanol
FOV	Field of view
ICP-MS	Inductively coupled plasma mass spectrometry
ID/g	Injected dose per gram tissue
IM	Intramuscular
IP	Intraperitoneal
IT	Intratumoral
IV	Intravenous
LCP	Lipid/calcium/phosphate
LPD	Lipid/protamine/DNA
MR imaging	Magnetic resonance imaging

	1-oleoyl-2-[12-[(7-nitro-2-1,3-benzoxadiazol-4-yl)amino]has
NBD-PC	beendodecanoyl]-sn-Glycero-3-Phosphocholine
NP	Nanoparticle
PDI	Polydispersity index
PEG	Polyethylene glycol
PET	Positron emission tomography
PK	Pharmacokinetics
PMCA	Plasma membrane Ca^{2+} pumps
ROIs	Region of interests
SPECT	Single-photon emission computed tomography
USPIO	Ultrasmall super-paramagnetic iron oxide

CHAPTER I

INTRODUCTION[1]

1.1 Clinical tumor imaging

Accurate and sensitive imaging of tumors and lymph node metastasis is important to the early clinical diagnosis and monitoring of therapeutic effects. During the past 20 years, advances in many basic sciences including chemistry, biology, physics, and engineering have made molecular imaging an autonomous scientific discipline that has extensive impact on clinical healthcare practices. Biomedical imaging is actually [2] playing an ever more important role in almost every phase of clinical cancer management [1-3]. These include cancer detection, staging [4], prognosis prediction [5], therapy planning [6], imaging-guided surgery [7, 8], therapy response evaluation [9], recurrence monitoring [10], etc. Many imaging techniques have the great advantage of being non-invasive, thus no surgery is required to obtain invaluable images. Current imaging systems frequently used in the clinic include magnetic resonance imaging (MR imaging), single-photon emission computed tomography (SPECT), positron emission tomography (PET), ultrasound, optical imaging, and X-ray systems, including computed tomography (CT).

---

[1] Parts of the introduction included in this chapter have been published in:

Tseng YC, Mozumdar S, and Huang L. (2009). Lipid-based systemic delivery of siRNA. Adv Drug Deliv Rev. Jul 25;61(9):721-31.

Tseng YC and Huang L. (2009). Self-assembled lipid nanomedicines for siRNA tumor targeting. J Biomed Nanotechnol. Aug;5(4):351-63.

These imaging systems vary in several physical properties such as sensitivity, temporal, and spatial resolution [11]. Nuclear medicine techniques, in particular, PET and SPECT, are the most sensitive achieving sensitivity between nanomole/kg and picomole/kg sensitivity and a resolution of ~1 mm. MR imaging has ~10 mmole/kg sensitivity and a resolution of up to ~50 micron (with a strong magnet). However, a major drawback of MRI is it could take hours of acquisition times to obtain a high resolution image. CT has millimole/kg sensitivity with a high resolution of up to several microns.

Optical imaging has great resolution but their clinical application have been limited to endoscopic, catheter-based devices and superficial imaging due to problems with scattering and absorption by the body tissues. However, success of optical imaging has been demonstrated in aiding surgical resection of tumor nodules [7, 8]. The tissue penetrating depth of fluorescent imaging could be improved to several millimeters by using long wavelength fluorophores or nanomaterials with excitation/emission wavelengths within the first or second near-infrared regions (0.75-0.9 μm, 1.1-1.4 μm, respectively) [12-16]. Two-photon excitation is another available technology that could be applied to enhance the penetrating depth of lights [17, 18]. Adopting Raman spectroscopy with tumor targeted nanoparticles and other promising strategies are the future directions of the field [19-21]. However, in terms of non-invasive deep tissue imaging, the capability of optical imaging is still limited.

1.2 SPECT/CT (Single-photon emission computed tomography)

Non-invasive imaging techniques using nuclear medicine, such as SPECT and PET, have the highest sensitivity among other imaging techniques [22, 23]. Among the radionuclides used in clinical practice, Indium-111 (^{111}In) is the second most widely used,

only surpassed by ^{99m}Tc. ^{111}In displays major decay at photon energy levels of 171.3 and 245.4 keV, within the ideal range of the detector device. The short, but sufficient half-life of ^{111}In (2.83 days) is also advantageous because prolonged exposure of normal organs to the radionuclide may cause undesired toxicity and should be prevented. Many studies have demonstrated *in vivo* imaging of tumors using SPECT/CT or PET/CT technique with various types of NPs [23-26].

SPECT has fairly good resolution of ~1 mm. However, SPECT images alone lack the anatomical details to provide meaningful surgical guidance. Several publications have demonstrated the advantages of fusing SPECT images with separately acquired CT images to address this issue [27-33]. Thus SPECT imaging machines have been commonly outfitted with a CT scanning component to form SPECT/CT imaging. Hybrid imaging systems could provide more detailed anatomical information, making them the future of molecular imaging [34].

1.3 Nanoparticles for therapy and imaging

Nanotechnology is an applied sciences field currently undergoing explosive development, especially in regards to medicine. The field, involves the creation, utilization, and design of materials and devices in the nanometer scale. There are several unique size-dependent physical and chemical properties (e.g. optical, magnetic, catalytic, thermodynamic, and electrochemical) of nanoparticles (NPs) [35]. NPs that have been developed for biomedical research can be roughly categorized into three categories: (1) inorganic NPs including quantum dots, iron oxide NPs, and gold nanostructures, (2) polymeric NPs such as dendrimers and amphiphilic NPs, and (3) lipid NPs, including liposomes, solid lipid NPs, and core-supported lipid NPs (e.g. LPD

(Lipid/Polycation/DNA) [36-39] and LCP (Lipid/Calcium/Phosphate) NPs [40-42] developed in our lab). In addition to these, the oncological applications of carbon nanotubes and nanodiamonds as novel materials have also been explored [43-45].

The high payload of the therapeutic agent and favorable pharmacokinetics and consequent reduced toxicity of the cargo drug are two advantages of using NPs as a delivery system. Furthermore, their multi-functionality [24], preferential accumulation in the tumor through the enhanced permeability and retention (EPR) effect [46, 47], and the enhanced binding with target cells due to ligand multivalency [48] are also advantages of this type of delivery system. Chapter 1.3.2-1.3.4 introduces the EPR effect and targeting ligands. With the capability of being multifunctional, NPs could carry therapeutics with contrast imaging agents (i.e., theragnostics) [49]. Also, due to their larger-size, NPs can often produce high signal:background ratios, which is the key to achieving satisfactory imaging results. However, avoiding clearance by the mononuclear phagocyte system (MPS), especially in the liver (Kupffer cells) [50] and spleen, is the first requirement for efficient delivery with NPs.

1.3.1 MPS clearance and PEGylation

Nanoparticles need to stay in the blood circulation long enough to overcome the kinetic barrier to extravasate from the leaky tumor vasculature [51]. The primary elimination mechanism for nanoparticles is clearance via the MPS. The major reason why unprotected NPs are prone to clearance by the MPS is because opsonins such as IgM, IgG, fibronectins, or complement C3 attached to the surface of NPs can attract phagocytic cells. This clearance by the MPS is the major obstacle for almost every colloidal NP. One common strategy first demonstrated in stealth liposome technology is

to use surface grafted carbohydrate or polyethylene glycol (PEG) to protect the particle and shield the particle's surface charges [52]. Studies have shown that PEGylated colloids [53, 54] and stealth liposomes [37] could stay in the blood circulation for up to 6–10 h in mice and 40 h in humans [55].

1.3.2 Enhanced permeability and retention (EPR) effect

Tumor cells are those that rapidly differentiate and grow. A large amount of nutrients is required for tumor growth. Angiogenesis as induced by growth factors including vascular endothelial growth factor (VEGF), is also important for tumor growth [56]. Neo-vasculatures in the tumor are usually leaky and not well organized. However, the degree of leakiness is highly tumor dependent and could vary significantly between tumors. Factors including the site and type of the tumor and the degrees of growth and regression lead to different degrees of vascular leakiness. Matsumura and Maeda [57] discovered that due to the leakiness of the vasculature in solid tumors, macromolecules and colloidal nanoparticles that are too big to penetrate normal blood vessels could extravasate from these leaky vasculatures and preferentially accumulate at the tumor site; termed the EPR effect. Lacking lymphatic drainage might also contribute to the enhanced retention effect [57-60].

To take advantage of the EPR effect, nanoparticles must be within an optimal size range. Although the EPR effect has been demonstrated in humans [61-63], not all human tumors are equally leaky. The optimum diameter for liposome-mediated drug delivery was determined to be around 100 nm [64]. However, this could be due to the fact that this is the pivotal size for long circulating liposomes. Smaller nanoparticles (~25 nm) have been shown to penetrate tumors better than larger nanoparticles [65].

However, the penetration of smaller nanoparticles is still highly dependent on the leakiness of the tumor vasculature.

1.3.3 Targeting ligands

The EPR effect is important in guiding nanoparticles to the tumor tissues, but is not enough to deliver siRNA into the cancer cells. Two physical barriers remain, the plasma and endosome membranes, which prohibit siRNA from entering the cytoplasm. Drugs or siRNA outside of the cancer cells are not bio-available and show no therapeutic effect. Nanoparticles with a structure too stable may stay in the tumor extracellular matrix without releasing payload drugs. For example, a stealth liposomal-cisplatin formulation (SPI-077) accumulated efficiently at the tumor site, but showed minimal therapeutic effect compared to free cisplatin [66]. In order to prompt cancer cells to take up nanoparticles, targeting ligands are needed for triggering receptor mediated endocytosis. There are various types of targeting ligands being used for tumor targeting, including peptides, proteins, antibodies (Fab, scFv, etc.), aptamers, and small molecular weight ligands, etc.

1.3.4 Anisamide and folic acid as targeting ligands

Small molecule ligands that have good binding affinities and specificities are also suitable for tumor targeting, although they are relatively rare. Such ligands are easy to synthesize, more tolerant to chemical modification/conjugation, have a low immunogenicity, and are stable enough for long-term storage, making them preferable over small peptides, proteins and antibodies. Folic acid, a vitamin, is the high affinity natural ligand for the folate receptor which is over-expressed in a wide range of human

cancers, including ovary, lung, breast, endometrium, kidney, and brain cancers. Protein toxins, chemotherapeutic agents, oligonucleotides, radioimaging/therapeutic agents, MRI contrast agents, and liposomes [67] have all been modified with folic acid to enhance their targeting of various tumors [68-70]. Similarly, anisamide [71] and haloperidol [72, 73] are small molecule ligands for use in targeting cancer cells that over-express the sigma receptor. These include melanoma, non-small cell lung carcinoma, breast tumors of neural origin, and prostate cancers [72, 74-76]. The LPD tumor targeting work done in our lab focused on anisamide as the targeting ligand [36-39].

1.3.5 Radiolabeling of Nanoparticles with ^{111}In

Radiolabeling is considered the most quantitative method of labeling in the field of drug delivery in cases where appropriate radiolabeling strategies are used. The major advantage of radiolabeling is the general lack of background signal in the images produced. The *in vivo* administration of radiolabeled NPs not only provides accurate biodistribution profiles and PK studies of the NPs but can also be used for SPECT/CT or PET/CT imaging. ^{111}In is convenient for studying NPs because of its half-life (2.83 days), which is both long enough for PK evaluations and short enough to reduce safety concerns.

There are several approaches to radiolabeling NPs, including (1) directly labeling the NP surface, (2) functionalizing the surface with a chelater for labeling, and (3) encapsulating radionuclides in the NPs [22]. Strategy (2) is the most commonly used in labeling with ^{111}In. DTPA (diethylene triamine pentaacetic acid) is the chelating agent of choice in this case. However, DOTA (1,4,7,10-tetraazacyclododecane-1,4,7,10-tetraacetic acid) can form highly stable complexes with various radionuclides (e.g. ^{111}In,

^{177}Lu, $^{86/90}$Y, $^{67/68}$Ga, and ^{64}Cu) and thus has become popular as a universal chelater [77]. DTPA or DOTA could be bound to PEG to acheive surface functionalization of NPs [53, 78]. Unfortunately, this strategy is not compatible with LCP NPs, most likely due to the destabilization of the LCP core by the chelation of calcium. Since ^{111}In can easily be formulated into the LCP core (demonstrated in Chapter 2), ^{111}In labeling through encapsulation was chosen as the method to be used.

The chelation of ^{111}In on the NP surface has been reported to induce accumulation of ^{111}In signal in the bladder [26, 78]. There is a concern regarding loss of ^{111}In chelating due to the competition or decomposition of NPs leading to the release of the ^{111}In-chelator complex. Functionalization may also affect the surface properties of NPs that could lead to the alteration of the biodistribution behaviors of NPs. Therefore, labeling LCP NPs with ^{111}In via encapsulation should be more reliable.

1.4 LCP (lipid/calcium/phosphate) nanoparticles

The LCP NP developed in this lab demonstrates superior efficiency in siRNA delivery [40-42]. Figure 1.1 illustrates the preparation scheme of LCP NPs. Utilizing microemulsion technology, two microemulsions of $CaCl_2$ and Na_2HPO_4 were formed and mixed to create the calcium-phosphate (CaP) nano-precipitate cores. CaP cores were coated with a single dioleoylphosphatydic acid (DOPA) layer. The phosphate head-group of DOPA provides a strong binding interaction with the CaP cores and prevents aggregation. The acyl chain of DOPA provides a hydrophobic surface that allows extensive wash and storage in $CHCl_3$. Following the washing, the cores could be further with the outer-leaflet lipid of choice to form an asymmetric lipid bilayer. For example, cationic 1,2-dioleoyl-3-trimethylammonium-propane (DOTAP) lipid was often used as

outer leaflet for its endosome destabilization activity. Neutral dioleoylphosphatidylcholine (DOPC) on the other hand, provided prolonged circulation time thus was used for tumor and lymph node imaging purpose after intravenous injection

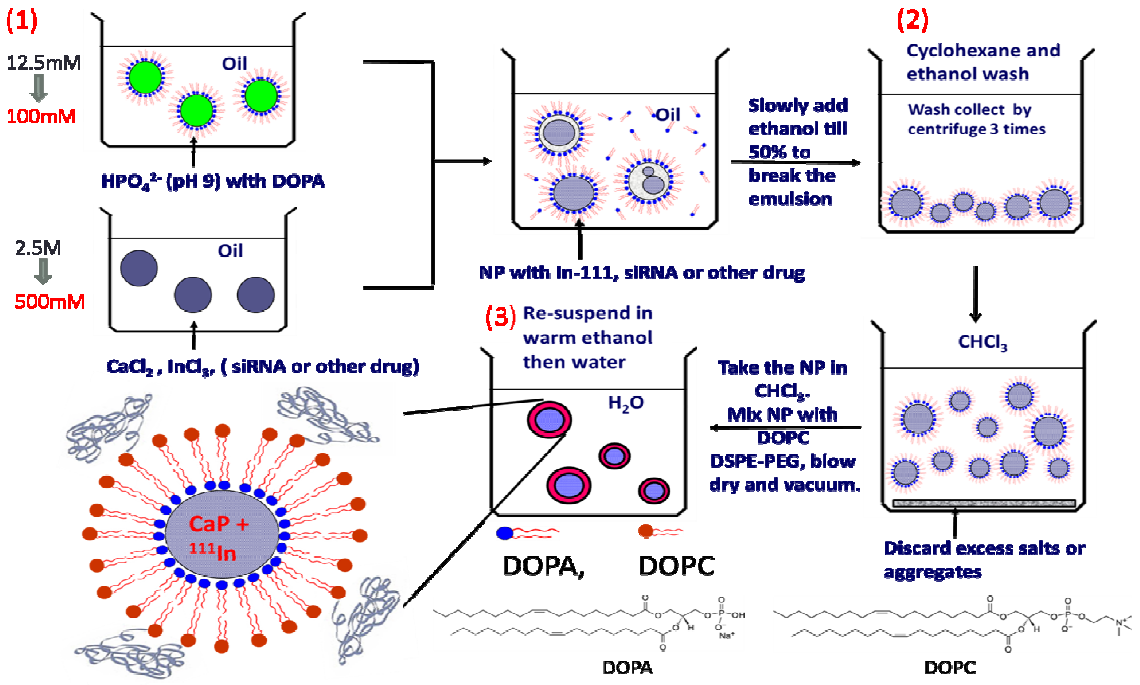

Figure 1.1 Cartoon illustration of LCP NP preparation.

Cartoon was modified from previous publication by Li et al., (2012) [40]. Major modifications for ^{111}In loading were marked in red and will be discussed in detail in Chapter 2.

The lipid bilayer of the LCP NPs is strongly supported by the interaction between the phosphate head group of the inner leaflet lipid DOPA and the CaP nano-precipitation core. The supported lipid bilayer enables grafting of a high density of DSPE-PEG$_{2000}$ (1,2-distearoyl-sn-glycero-3-phosphoethanolamine-N-poly(ethylene glycol)2000) that cannot be achieved with conventional liposomes, providing superior protection against uptake by the MPS [79]. Targeting ligands could be added onto the tip of PEG molecules.

Similar to the well-established calcium phosphate-mediated transfection method for plasmid DNA delivery [80], the CaP core in our LCP NPs will form precipitates with siRNA (or DNA). These CaP-siRNA or CaP-DNA co-precipitates are acid sensitive. After cellular internalization, the co-precipitates will dissolve in the acidic endosomal environment to induce an osmotic lysis and thus release the trapped siRNA (or DNA). This releasing mechanism was designed to improve the release of siRNA into the cytoplasm, which was demonstrated by the punctate FITC-siRNA distribution pattern of LPD NPs and the homogeneous FITC-siRNA distribution pattern of LCP NP in the cytoplasm [40].

The dissolution of the CaP core increases the osmotic pressure in the endosome, aiding the process of escape from the endosome. Figure 1.2 illustrated the proposed releasing mechanism. After cellular internalization by receptor mediated endocytosis, the DSPE-PEG will shed and LCP core will decompose due to acidic environment in the endosome. Two endosome escape mechanisms were shown: (1) cationic lipid will interact with anion endosomal membrane to destabilize endosome membrane; (2) the increased osmotic pressure caused by dissolved Ca^{2+} and PO_4^{3-} ions will help to burst the endosome. Thus the siRNA, chemical drug, and cDNA will be released in the cytoplasm. The cDNA carried by an oligo-arginine peptide into the nucleus for transcription (Hu et al., manuscript in submission) was also shown.

The mechanism of CaP dissolution and endosome escape was demonstrated through the use of a calcium sensing dye, fura-2, to visualize the elevated cytoplasmic calcium concentrations [81]. However, the elevated calcium concentration is only transient and not toxic to cells (Chapter 2.7).

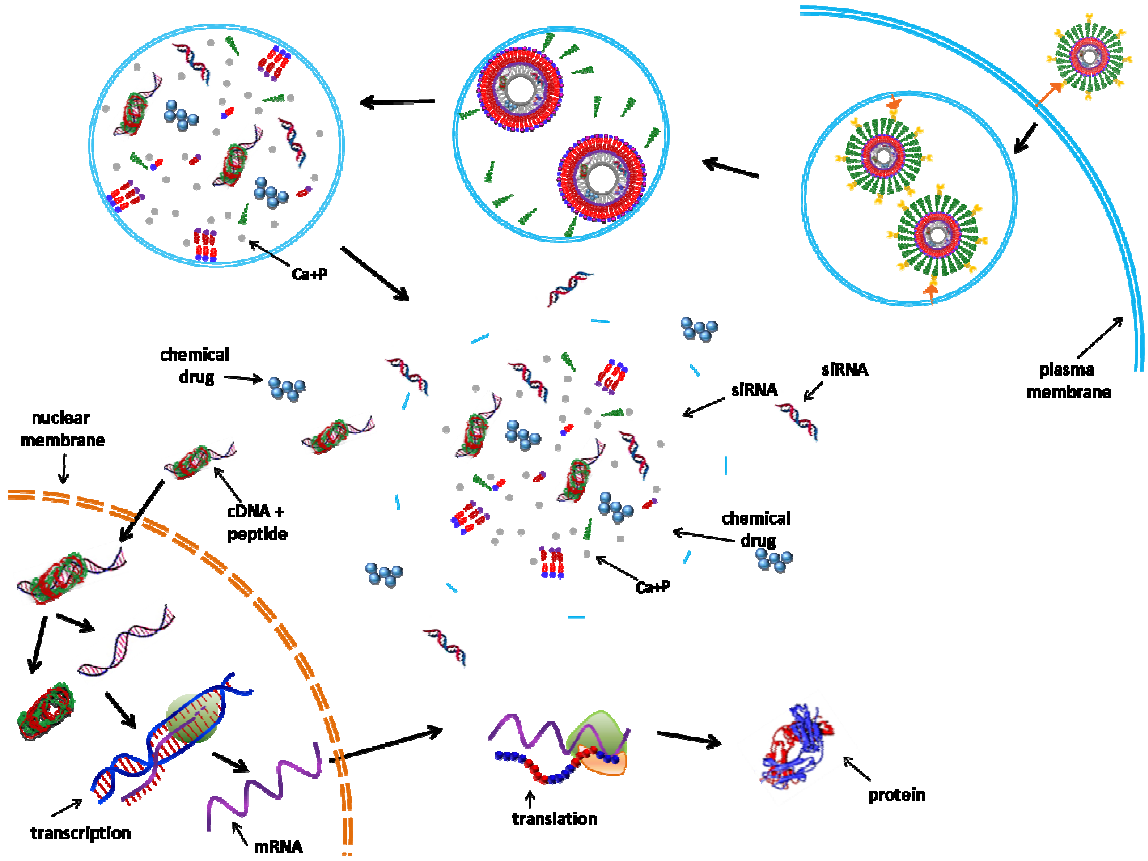

Figure 1.2 Cartoon illustration of the drug releasing mechanisms of LCP NP.

Endosome escape mechanism and the releasing of therapeutics including siRNA, chemical drug, and cDNA were shown. (Cartoon drawn by Bethany DiPrete)

Based on the mechanism of formation of the CaP core, we hypothesized that any drug or radionuclide that can form co-precipitates with CaP has the potential to be formulated into LCP NPs. For example, a variety of anti-viral nucleoside analogue drugs [82-85] could be entrapped via a similar strategy as gemcitabine mono-phosphate (Zhang et al., manuscript in submission). Since indium (In) can form precipitates with phosphate efficiently (Ksp of $InPO_4$ = $2.3x10^{-22}$) in a manner similar to that of calcium (Ksp of $Ca_3(PO_4)_2$ = $1.0x10^{-25}$), we hypothesize that ^{111}In will be a good candidate to add to LCP NP formulation to provide *in vivo* imaging capabilities and could be used for biodistribution study.

CHAPTER II

FORMULATING ^{111}IN INTO LCP NANOPARTICLE FORMULATION

2.1 Introduction

As mentioned in Chapter 1.4, it was hypothesized that we should be able to formulate ^{111}In into LCP to form ^{111}In-LCP by Ca-In-P co-precipitation. However, the formulation was designed to encapsulate siRNA. The $CaCl_2$ and Na_2HPO_4 concentrations in the original LCP formulation were 2.5 M and 12.5 mM, respectively [40]. The high $CaCl_2$ concentration used in this formulation is the commonly used concentration in the calcium phospate plasmid transfection method [80]. The high calcium concentration guarrentees that the calcium will be in excess and the formed calcium-phosphate-plasmid complex will have a positive surface charge. This positive surface charge is critical to the transfection due to the facilitation of the interaction between the calcium-phosphate-plasmid complex with the cell membrane, which has negative surface charge. Excess calcium is also needed for LCP formulation; the interaction of DOPA and the CaP cores relies on excess calcium to ensure that the core surface is mainly calcium and not phosphate. However, since ^{111}In will compete with calcium for phosphate, too much excess calcium will impede the formulation of ^{111}In into the core. Other improvements in LCP formulation are still needed to ensure a thourough lipid coating and the partocles' *in vivo* performance. This chapter will describe the major modifications made to LCP formulation that led to the successful imaging results in Chapter 3.

2.2 Adjusting $CaCl_2$ and Na_2HPO_4 concentrations for ^{111}In loading

The general procedure for LCP preparation was established by Li et al. [40]. In order to efficiently formulate ^{111}In into the CaP core; some major adjustments have been made to this procedure for our experiments (Figure 1.4). Since ^{111}In will compete with calcium for phosphate, the $CaCl_2$ concentration has been reduced from 2.5 M to 500 mM and the Na_2HPO_4 concentration (pH 9.0) has been increased from 12.5 mM to 100 mM. Due to the 8-fold increase in the Na_2HPO_4 concentration, the total microemulsion working volume was able to be reduced to 1/8 accordingly for the same preparation size. This reduction in volume would be beneficial for future scale-up.

The concentration adjustments did not only enhance the efficiency of encapsulating ^{111}In by reducing calcium competition, but also encouraged the formation of $InPO_4$ and not $In(OH)_3$. The formation of $InPO_4$ (same as $Ca_3(PO_4)_2$) was desired because for each PO_4^{3-} ion, there are three delocalized negative charges on four oxygens that allow interaction with multiple In^{3+} and Ca^{2+} ions. These interactions build a framework structure for a condensed LCP core. In the case of the OH^- ion, the single negative charge did not allow the formation of the framework structure and was not ideal for creating the core.

Table 2.1 Ksp values of $Ca(OH)_2$, $Ca_3(PO_4)_2$, $In(OH)_3$, and $InPO_4$.

Ca(OH)2	Ca3(PO4)2	In(OH)3	InPO4
5.5×10^{-6}	1.0×10^{-25}	1.3×10^{-37}	2.3×10^{-22}

Table 2.1 listed the Ksp values of of $Ca(OH)_2$, $Ca_3(PO_4)_2$, $In(OH)_3$, and $InPO_4$. Consider the starting condition upon mixing of calcium and phosphate microemulsions:

With 50 mM Na_2HPO_4, pH 9.0:

$Ca(OH)_2$: $[Ca^{2+}][10^{-5}]^3 = 5.5 \times 10^{-6}$ $[Ca^{2+}] = 5.5 \times 10^{9}$

$Ca_3(PO_4)_2$: $[Ca^{2+}][5 \times 10^{-2}]^3 = 1.0 \times 10^{-25}$ $[Ca^{2+}] = 4 \times 10^{-23}$

$In(OH)_3$: $[In^{3+}][10^{-5}]^3 = 1.3 \times 10^{-37}$ $[In^{3+}] = 1.3 \times 10^{-22}$

$InPO_4$: $[In^{3+}][5x10^{-2}] = 2.3 \times 10^{-22}$ $[In^{3+}] = 4.6 \times 10^{-21}$

With 6.25 mM Na_2HPO_4 pH 9.0:

$InPO_4$: $[In^{3+}][6.25x10^{-3}] = 2.3 \times 10\text{-}^{22}$ $[In^{3+}] = 3.68 \times 10^{-20}$

This starting condition indicates the formation of $Ca_3(PO_4)_2$ was favored over the formation of $Ca(OH)_2$. There was no concern that calcium would form $Ca(OH)_2$, only $Ca_3(PO_4)_2$. On the other hand, $In(OH)_3$ seemed to be favored slightly over $InPO_4$. Increasing the concentration of Na_2HPO_4 in the microemulsion from 12.5 mM to 100 mM encouraged the formation of $InPO_4$; this calculation was based on the starting condition. As one would expect, the mixing of the two microemulsions caused a decrease in the phosphate concentration as the CaP precipitate formed. However, how the $[OH^-]$ concentration was altered in the mixed micromulsion is more difficult to examine. To determine the change, 500 mM $CaCl_2$ solution was mixed with 100 mM Na_2HPO_4 solution in bulk condition. Massive CaP precipitation formed immediately and the pH was measured as 4.6. This dramatic decrease in the pH value can be explained by the

following equation:

$$[HPO_4^{2-}] \rightleftharpoons [H^+] + [PO_4^{3-}]$$

As Ca^{2+} and In^{3+} consume PO_4^{3-} to form $Ca_3(PO_4)_2$ and $InPO_4$, the equilibrium is shifted to the right, generating a significant amount of H^+ that neutralizes OH^- and lowers the pH value. The formation of CaP was the most dominant reaction since Ca^{2+} and PO_4^{3-} were the most abundant ion species in the mixture. The pH value should drop immediately and provide for minimal $In(OH)_3$ formation. Based on this Ksp calculation, we hypothesized that the ^{111}In should mainly form $InPO_4$ and could be formulated into the LCP core efficiently.

2.3 The preparation of ^{111}In-LCP cores

^{111}In-LCP cores were prepared using the previously described method by Li et al. [40] with some modifications (Figure 1.4). Two water-in-oil microemulsions were prepared: 1) a calcium emulsion: $^{111}InCl_3$ (in 0.05 N HCl, PerkinElmer, Inc.) was premixed with $CaCl_2$ to make a final 50 µL of 500 mM $CaCl_2$ in 4 mL of cyclohexane oil phase (cyclohexane/Igepal CO-520 = 71/29, v/v), and 2) a phosphate emulsion: a sufficient amount of 0.05 N NaOH was added to pH 9.0 Na_2HPO_4 (to neutralize the extra HCl in the calcium emulsion) to make final 50 µL of 100 mM Na_2HPO_4 also in 4 mL of cyclohexane oil phase. DOPA (92.5 µL 34.6 mM in chloroform, Avanti Polar Lipids, Inc.) was also added to the phosphate emulsion to form the inner leaflet lipid.

After mixing the two microemulsions for 40 min, 8 mL of absolute ethanol was added to break the microemulsion system. The mixture was stirred for another 30 min.

Then, the mixture was centrifuged at 12,500x g for 15 min to collect the ^{111}In -LCP cores.

The cores were then washed once with 10 mL absolute ethanol to remove residual surfactants. Washing with 1.2 mL cyclohexane and an addition of 1.4 mL absolute ethanol removed residual DOPA. Finally, the cores were washed with 2 mL of absolute ethanol to ensure the removal of cyclohexane. After all washes, the pellets were dispersed in 250 µL of chloroform. The product was centrifuged at 10,000x g for 5 min. Precipitates containing excess salts and aggregates were discarded and the supernatant containing LCP cores was collected and stored in a glass vial at -20 ℃.

In the original method described by Li et al. [40], the LCP cores are to be washed extensively only with a large volume of ethanol (EtOH). The use of cyclohexane in our method was inspired by the observation that after chloroform dispersion of the core, if one evaporated the chloroform the LCP core pellets were no longer suspendable or able to be separated in EtOH. The LCP cores bound tightly to each other and the walls of the eppendorf tube. We postulated that since chloroform was a stronger hydrophobic organic solvent than EtOH, it may more efficiently separate and remove excess DOPA and surfactants on the core. Furthermore, chloroform may also make the core surface truly hydrophobic, creating tight binding between the cores that EtOH could not break. However, chloroform has a higher density (1.483 g/mL) than cyclohexane (0.779 g/mL), Making cyclohexane more desirable for use in washing processes involving centrifugation as the collection method. The ability of cyclohexane to remove excess DOPA is demonstrated in Table 2.2. As indicated, EtOH has little power to wash away excess DOPA (a small amount of NBD-PA fluorescent was used as marker). However, cyclohexane was able to further wash away excess DOPA. Note that some ^{111}In was also lost during the cyclohexane washing.

Table 2.2 Washing power of cyclohexane.

	First supernatant	EtOH	Cyclohexane/ EtOH	EtOH	In NPs
NBD-PA	66.5%	0.4%	12.9%	0.3%	--
^{111}In	20.6%	0.7%	17.7%	0	30.7%

This additional cyclohexane washing also resulted in significant improvement in the quality of coating of the LCP surface (indicated by a clearer final LCP suspension) and the *in vivo* biodistribution profiles. Before using the cyclohexane washing, the spleen accumulation was high probably due to agglomerated LCP (Figure 2.1A). The cyclohexane washing significantly reduced spleen accumulation and enhanced lymph node accumulation (Figure 2.1B). The improved biodistribution pattern is similar to those of several of the best performing SPECT/CT or PET/CT imaging NPs, including gold NPs [53, 78] and polymeric micelles [86]. These results indicated that the coating of LCP surface might not be ideal with the original ethanol washing and outer-leaflet coating method. We observed turbidity in the suspension before implementing the cyclohexane wash, which was resolved following the use of this improved technique.

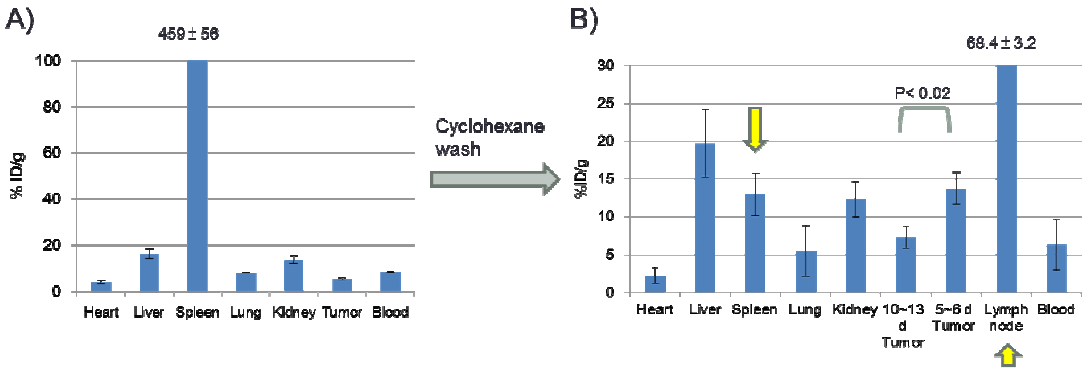

Figure 2.1 Improved biodistribution pattern of S-LCP after cyclohexane wash.

A) LCP biodistribution pattern before the cyclohexane washing improvement. B) LCP biodistribution pattern after the cyclohexane washing improvement. The result of B) is actually the biodistribution data after the SPECT/CT imaging which will be described in Chapter 3.1.

2.4 Coating with an outer leaflet

To form the coating of the outer leaflet, 100 μL of 20 mM cholesterol, 100 μL of 20 mM DOPC (Avanti Polar Lipids, Inc.) or DOTAP (Avanti Polar Lipids, Inc.), and 50 μL of 20 mM of 1,2-distearoyl-sn-glycero-3-phosphoethanolamine-N-poly(ethylene glycol)2000 (DSPE-PEG_{2000}, Avanti Polar Lipids, Inc.) were mixed with the LCP cores in a glass vial. After the complete removal of the $CHCl_3$ using a stream of nitrogen and vacuum desiccation for 1 h, the cores were suspended in 100 μL of pre-warmed absolute alcohol (55 ℃) and dispersed in a 1 mL pre-warmed aqueous solution containing 5% dextrose.

The amount of lipid required for coating with an outer leaflet was experimentally determined using sucrose gradient centrifugation. A PC labeled with green flourescence, NBD-PC (1-oleoyl-2-[12-[(7-nitro-2-1,3-benzoxadiazol-4-yl)amino]dodecanoyl]-sn-Glycero-3-Phosphocholine), was mixed with DOPC to label the outer leaflet. The fluorescent labeled LCP NPs were loaded in the middle of an ultra-centrifugation tube containing a sucrose density gradient ranging from 0% to 60% (w/w) to allow flotation of the excess lipid and the sedimentation of dense LCP NPs. After ultra-centrifugation at 337,000x g for 4 h, excess lipids that were not associated with LCP NPs floated to the upper part of the gradient and could be separated from the dense LCP NPs which formed a sharp band right above the 60% gradient layer (Figure 2.2). By analyzing the NBD intensities of the floated excess lipids and that of the LCP, the optimum amount of

outer leaflet lipids to be used for coating was determined to be 1.56 folds of the inputted inner leaflet, DOPA.

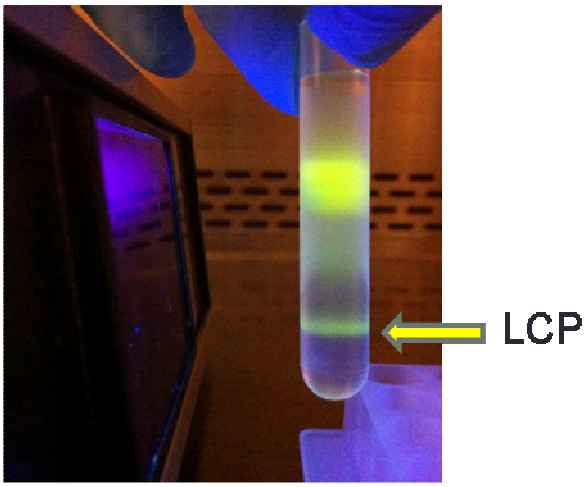

Figure 2.2 Purify LCP NPs using sucrose gradient centrifugation.

A 4 mL Beckman polyallomer ultra-centrifugation tube was used for the 60% to 0% sucrose gradient. The NBD fluorescent was excited with a hand-held UV lamp for observation.

2.5 Tuning LCP nanoparticle size

The LCP NP made with the modified $CaCl_2$ and Na_2HPO_4 concentrations and the original Igepal surfactant system (cyclohexane/Igepal CO-520 = 71/29, v/v) was small in size. The CaP core was ~10 nm in diameter and the final LCP NP coated with the outer leaflet lipids was ~25 nm (Figure 2.3A), which is consistent with previous observations [40, 41]. These small NPs have been termed S-LCP. The invention of the LCP NPs illustrated for the first time that a small NP with a lipid bilayer coating could be created while also maintaining a well-PEGylated surface. For example, the LPD NPs previously developed in this lab, which also had a supported lipid-bilayer coating, had an average size of around 100 nm [38]. Although there are extensive studies regarding the subject of NP biodistribution within this small size range, the studies mainly focus on iron oxide

NPs, gold NPs, polymeric micelles, and quantum dots with different surface protection coatings [53, 87]. There is no literature that characterizes the *in vivo* biodistribution behavior of well-PEGylated, lipid-bilayer-coated NPs in such a small size range. In order to study this concept, an enlarged version of LCP (L-LCP) was developed and the *in vivo* performance of NPs of both sizes was also evaluated for comparison.

As shown in Figure 2.3, by adjusting the microemulsion surfactant system, LCP core size could be tuned from ~10 nm and ~50 nm in diameter. When mixing the Igepal system (cyclohexane/Igepal CO-520 = 71/29, v/v) with the Triton system (cyclohexane/hexanol/Triton X-100 = 75/10/15, v/v/v) at a 1:1 or 1:3 ratio, particles had become progressively larger (Figure 2.3A). When using an Igepal:Triton ratio at 1:7, the ^{111}In-LCP core was significantly enlarged to ~50 nm. This larger LCP with a final outer-leaflet coated size of ~65 nm have been termed L-LCP in this thesis. Both S- and L-LCP were outer leaflet coated with DOPC/Cholesterol/DSPE-PEG2000 (2/2/1 molar ratio) for most of the experiments done in this thesis unless otherwise specified.

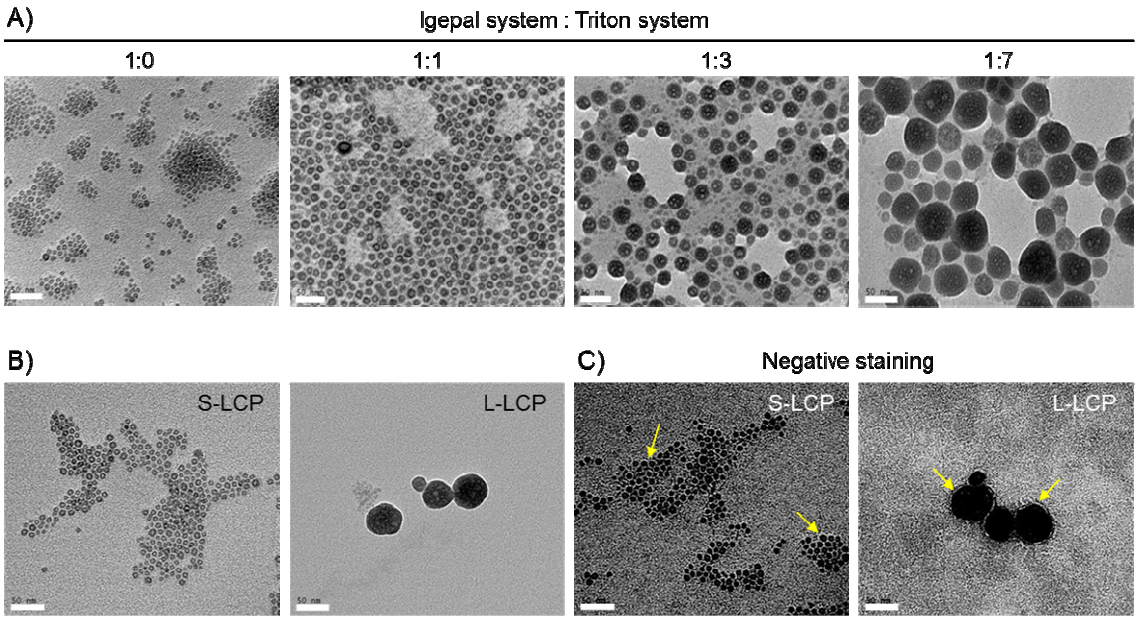

Figure 2.3 TEM images of LCP NPs

A) TEM images of ^{111}In -LCP core made with different Igepal system to Triton system mixing ratio. S- and L-LCP were made by Igepal system to Triton system ratio 1:0 and 1:7, respectively. B) TEM images of S- and L-LCP after outer leaflet coating. C) Negative staining of S- and L-LCP to show the lipid coating. (Scale bars = 50 nm)

TEM images of the final S- and L-LCP after outer leaflet coating showed that both S- and L-LCP were well separated individual particles (Figure 2.3B). The lipid membrane coating of S- and L-LCP was further visualized by negative staining using uranyl acetate (Figure 2.3C).

Other strategies were implemented to try to enlarge LCP size, but they failed. These strategies included adjusting w:o ratio, modifying concentrations of $CaCl_2$ and Na_2HPO_4, prolonged incubation, and stepwise adding $CaCl_2$. Heating the microemulsion system of L-LCP with water bath to 65℃ could furth er increase the particle size to around 100 nm. However, the cores made using this method were less homogeneous as

indicated by the presence of a number of smaller LCP cores observed in the TEM images. (Figure 2.4).

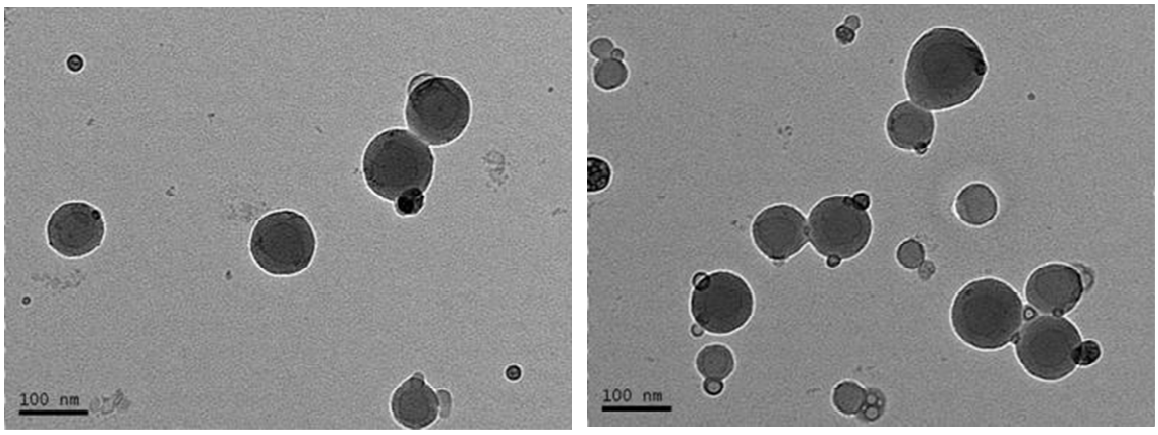

Figure 2.4 TEM images of LCP core made with Igepal system/Triton system = 1/7 in water bath at 65℃.

2.6 Characterizing LCP nanoparticles

2.6.1 Size and zeta-potential measurement by dynamic light scattering

After coating with the outer leaflet, the final LCP was purified using the aforementioned sucrose-gradient, centrifugation method (described in Chapter 2.4) in order to prepare them for analysis with dynamic light scattering (DLS) using a Malvern ZetaSizer Nano series instrument (Westborough, MA). Since excess lipids may form liposomes or micelles that could interfere with DLS analysis, purification was necessary to ensure correct measurements. The DLS analysis results revealed a NP population with a fairly uniform S-LCP size (~25 nm) with a polydispersity index (PDI) below 0.3 and a zeta potential of approximately -20 mV. L-LCP, on the other hand, was around 67 nm in size with a PDI of ~0.4 and a zeta potential around -18 mV (Table 2.3).

Table 2.3 Characterization of S-LCP and L-LCP

	DNA oligo entrapment [a]	^{111}In entrapment [b]	Size/PDI [c]	Zeta potential [c]	Calcium/Phosphate ratio of the LCP core [d]
S-LCP	64.4 ± 4.4%	30.7 ± 4.1 %	25.3 ± 1.9 nm/0.3	-19.9 ± 4.1 mV	1.01 ± 0.04
L-LCP	29.2 ± 0.5%	32.3 ± 2.2 %	67.2 ± 2.0 nm/0.4	-18.0 ± 2.0 mV	0.89 ± 0.03

[a] determined by tritium labeled DNA oligo and liquid scintillation counting (N=3)

[b] determined by ^{111}In gamma counting (N=4)

[c] measured by dynamic light scattering (N=3)

[d] analyzed by ICP-MS. (N=3)

2.6.2 Determine oligo entrapping efficiency with ^{3}H-labeled DNA oligo

Due to issues with stability and in order to reduce costs, DNA oligo was used as a surrogate for siRNA. ^{3}H labeling of oligonucleotides was prepared using a method of hydrogen exchange, with $^{3}H_2O$ at the C8 positions of the adenine and guanine groups of the oligonucleotides (described by Graham et al.) [88]. One-hundred nmol (1.224 mg) of DNA oligo was lyophilized and put in PBS combined with 0.1 mM EDTA. Two hundred µL of $^{3}H_2O$ containing 8.3 uL β-mecaptoethanol was added and allowed to incubate at 90℃ for 6 h. Then the unexchanged $^{3}H_2O$ was removed via lyophilization. The product was resuspended in 1 mL of regular water and incubated for 1 h at room temerature to allow the rapidly exchangeable protons to dissociate. This lyophilization/resuspension process was repeated for three cycles. The final product was passed through a Centri-Spin oligo purification column (Prince Separation) to remove the PBS salt and EDTA.

To determine oligo entrapment efficiency, a trace amount of ^{3}H-labeled DNA

oligo was mixed with non-labeled DNA oligo to make the LCP cores. Using scintillation counting, it was determined that S-LCP could entrap DNA oligo at an efficiency of ~60%, which was not affected by the presence of ^{111}In. DNA entrapment of L-LCP was also unaffected by the presence of ^{111}In, but could only entrap ~30% of the DNA oligo (Table 2.3). The reason for this difference in entrapment is not fully understood.

2.6.3 Determine ^{111}In entrapping efficiency

The ^{111}In entrapment efficiencies of both S- and L-LCP were around 30%, determined by gamma counting (Table 2.3).

2.6.4 Determine calcium/phosphate ratio in the LCP core

Inductively coupled plasma mass spectrometry (ICP-MS) was used to analyze the LCP core compositions. For both S- and L-LCP, the Ca/P ratio were about 1, which was different from that of the naturally occurring hydroxyapatite (Ca10(PO4)6(OH)2, Ca/P = 1.67), suggesting an amorphous CaP precipitation in the LCP (Table 2.3).

2.6.5 Conclusions

These characterization results of LCP indicated that the modifications made for efficient ^{111}In encapsulation did not significantly change the properties of the original LCP.

2.7 How does the cell manage calcium toxicity?

The dissolution of LCP core in the endosome is designed to release the drug (siRNA, plasmid, chemical drug, etc.) and increase the osmotic pressure to promote the bursting of the endosome and the consequential escape. The elevated cytoplasmic Ca^{2+} concentration has been demonstrated through a Fura-2 experiment [40]. Fura-2 is a ratiometric fluorescent Ca^{2+} sensitive dye. It was the first widely-used calcium indicator and remains very popular, especially in the field of neuroscience. The Ca^{2+} free Fura-2 excitation wavelength profile peaked at 380 nm. Upon Ca^{2+} binding, there is a blue-shift in the excitation peak to 340 nm. The emission wavelength remains unchanged at 510 nm.

Under physiological conditions, the Ca^{2+} concentration is ~1.2 mM extracellularly and ~0.1μM in the cytosol. The cytosolic Ca^{2+} concentration is associated with several cellular signaling events. Low to moderate Ca^{2+} concentrations (0.2-0.4 μM) triggers apoptosis, higher concentrations of Ca^{2+} (>1 μM) are associated with necrosis [89-93]. For this reason, it is necessary to address whether the Ca^{2+} delivered by LCP would be toxic to the cells.

The low cytosolic Ca^{2+} concentration was carefully regulated by several Ca^{2+} pumps on the plasma membrane, mitochondria, and endoplasmic reticulum (ER). Plasma membrane Ca^{2+} pumps (PMCA) consume ATP to extrude cellular Ca^{2+} with a high affinity, playing a major role in Ca^{2+} homeostasis and signaling. Inside of the cell, the mitochondria and ER are the two organelles where cells store Ca^{2+}. When there is any inward flux of Ca^{2+}, both the plasma membrane and the mitochondria will remove Ca^{2+} from the cytoplasm immediately. The endoplasmic reticulum, however, does not take up any more Ca^{2+} due to being already replete with Ca^{2+}. [94].

Based on the calcium homeostasis mechanism, we hypothesized that when cells take up LCP and release Ca^{2+} into the cytoplasm, the two major Ca^{2+} pumps on the plasma membrane and the mitochondria will rapidly respond to the elevated cytosolic Ca^{2+} concentration and prevent the cells from Ca^{2+} induced apoptosis or necrosis.

2.7.1 Design of *in vitro* Fura-2 experiment

Two specific Ca^{2+} pump inhibitors were selected to exam the hypothesis. The plasma membrane Ca^{2+} pump (PMCA) inhibitor, Caloxin 2A1, is a peptide (Val-Ser-Asn-Ser-Asn-Trp-Pro-Ser-Phe-Pro-Ser-Ser-Gly-Gly-Gly-NH_2, purchased from American Peptide Company) developed by using the phage display technology [95-97]. The mitochondrial calcium uniporter (MCU) specific inhibitor, Ru360 (EMD Millipore), is a cell-permeable, oxygen-bridged dinuclear ruthenium amine complex that binds to mitochondria with high affinity (K_d = 340 pM) and blocks Ca^{2+} uptake into mitochondria at IC_{50} = 184 pM *in vitro* [98, 99].

H460 human lung cancer cells were pre-loaded with Fura-2 AM (Molecular Probes) following manufacturer's protocol. After Fura-2 loading, H460 cells were treated with Ru360 at ~500 pM starting 30 min before adding S-LCP coated with DOTAP and was present throughout the entire ratio imaging experiment. The culture medium was switched to divalent cation-free PBS to avoid the interference of Ca^{2+} in the culture medium. Caloxin 2A1 at 1 mM was added 10 min before the addition of S-LCP and was presented throughout the entire ratio imaging experiment. The live cell ratio images were taken using an inverted Nikon ECLIPSE TE2000 microscope. This microscope was designed with a rapid-switch excitation shutter and multifunctional time lapse capability with dual cameras, ideal for Fura-2 experiments. A cell culture chamber with

temperature, humidity control, and 5% CO_2 supply was used for cell viability control. We recorded the ratio imaging video for 10 sec, paused for LCP addition, then recording was resumed for additional 8 min.

2.7.2 Results and discussion

During the ratio imaging, red pseudo color was applied to fluorescent signal detected with 380 nm excitation. Green pseudo color was applied when using 340 nm as excitation. Red and green channels were superimposed and adjusted to be in red color before adding LCP (Figure 2.5). It is important to add the LCP only when the cells are on the verge of transitioning from red to green. In the group without inhibitors, after adding LCP some cells turned green occasionally, indicating elevated Ca^{2+} concentration in the cytosol. Note that the cells were incubated with LCP throughout the imaging experiments. The uptake of LCP and the pumping of Ca^{2+} were both continuous processes. As a result, some cells actually switched color several times during the observation period.

As we hypothesized, when the Ca^{2+} pumps were inhibited by the two inhibitors, the cells lost their ability to cope with the elevated cytosolic Ca^{2+} concentration. The cells turned green immediately and rarely turned back to red. Even more, most cells started to lose their fluorescence indicating the loss of the Fura-2 dye. After imaging, we observed the morphology of the cells. Most of the cells were swollen, which is a typical sign of necrosis. Loss of cell membrane integrity is also a typical sign of necrosis. As indicated in Figure 2.5, only one inhibitor showed partial effect. PMCA was more important in managing the Ca^{2+} toxicity caused by LCP as Caloxin 2A1 alone seemed to have more effect than Ru360 alone. A control group using empty DOTAP liposome at the same DOTAP concentration as in LCP did not cause any color change (data not shown),

indicating that the observed Ca^{2+} concentration change was not due to the cationic lipid.

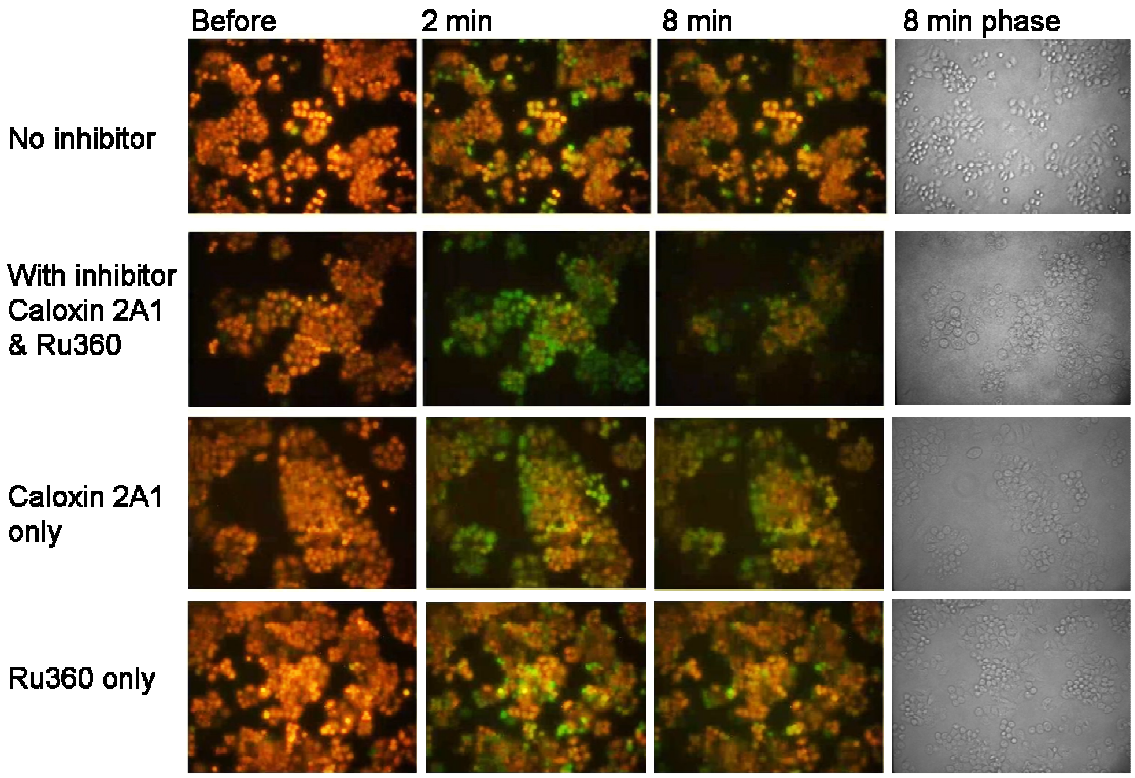

Figure 2.5 Calcium pumps are important for Ca^{2+} toxicity management

Shown here are stills taken from the recorded video at the indicated time points for four different treatment groups. Red color indicates low intracellular Ca^{2+} concentration under physiological conditions. Green color indicates elevated intracellular Ca^{2+} concentration. Phase contrast images taken at 8 min are included to show round, swollen cells.

The LCP concentration used in this ratio-imaging experiment was calculated as ~50% injected dose per gram tissue (ID/g) in the tumor for intravenous dosing. This accumulation level is rarely achievable *in vivo*. The H460 cells were exposed to LCP as a single layer cell culture, which is also a condition not achievable in the tumor. Thus, we

conclude that the Ca^{2+} delivered by LCP is unlikely to cause Ca^{2+} induced apoptosis or necrosis *in vivo*. Several *in vivo* studies delivering siRNA with the LCP formulation also reported minimum toxicities in the animal models [41, 42]. Nevertheless, we had proceeded to test the hypothesis *in vivo*.

2.7.3 Evaluating LCP induced Ca^{2+} toxicity *in vivo* with Ca^{2+} pump inhibitors

Next, we tested the Ca^{2+} induced toxicity in *in vivo* conditions. Nude mice bearing H460 xenografts on the right hind leg were used. The two Ca^{2+} pump inhibitors together were given by intratumoral (IT) injection. The mice were given injected with LCP coated 20% PEG and DOTAP either by intravenous (IV) or IT injection. At 2 h post injection, the mice were sacrificed and the tumors were fixed with formalin and sectioned for H&E staining. As Figure 2.6 indicates, there was no significant sign of necrosis in blank tumor, inhibitors only tumor, or tumor with IV injected 20% PEG and DOTAP coated LCP. Obvious cell necrosis was observed in the tumor received IT injection of inhibitors with either IV or IT injection of LCP coated with 20% PEG and DOTAP. An additional mouse received IT injection of both inhibitors and LCP coated with DOTAP but without PEGylation showed the most severe necrosis (Figure 2.6F). PEGylation of LCP was necessary for IV injection; un-PEGylated LCP did not accumulate in the tumor (data not shown). For IT injection, un-PEGylated LCP should interact more strongly with the tumor cells than the PEGylated LCP. Thus, the result of the *in vivo* experiment confirmed our hypothesis that no significant tumor cell necrosis could be induced by LCP unless the Ca^{2+} pumps of the tumor cells were blocked by inhibitors.

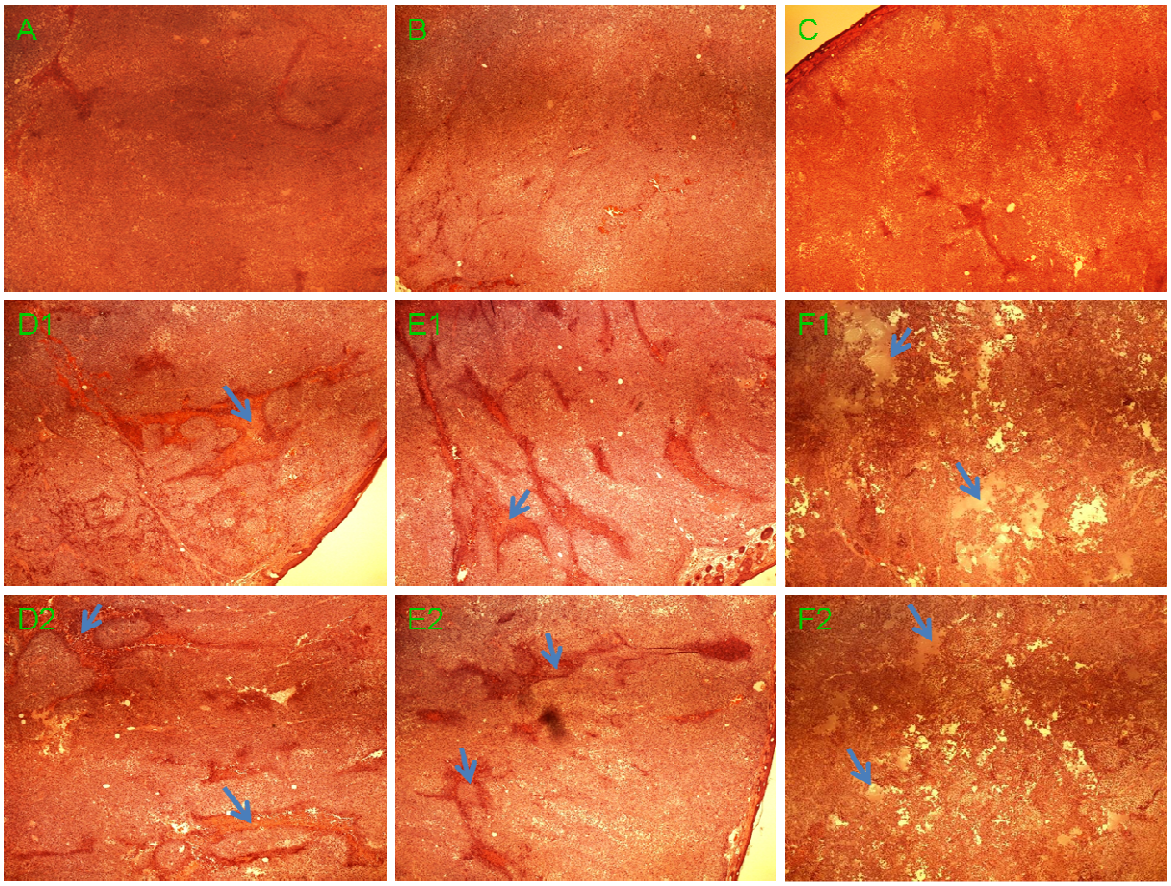

Figure 2.6 *In vivo* necrosis induced by LCP with Ca^{2+} pump inhibitors

H460 subcutaneous tumor sections with H&E staining showing that LCP toxicity was only observed in the presence of Ca^{2+} pump inhibitors. (A) Control H460 tumor without any treatment. (B) Tumor that has received an IT injection of two Ca^{2+} pump inhibitors. (C) Tumor that has received an IV injection of LCP. (D1, D2) Tumors that have received an IT injection of two Ca^{2+} pump inhibitors and an IV injection of LCP. (E1, E2) Tumors that have received an IT injection of two Ca^{2+} pump inhibitors and an IT injection of LCP. (F1, F2) Tumors that have received an IT injection of two Ca^{2+} pump inhibitors and an IT injection of LCP without PEGylation. Blue and black arrows indicate necrotic and severely necrotic regions, respectively.

2.7.4 Conclusion

This experiment concludes that in the normal condition, cells were able to manage the elevated cytosolic Ca^{2+} delivered by LCP by removing the Ca^{2+} with two major Ca^{2+} pumps on the plasma membrane and mitochondria (Figure 2.7). The elevated Ca^{2+} concentration was only a transient event and was not toxic to the cells. Previous tumor siRNA delivery and liver hepatocyte gene delivery projects done in this lab also demonstrated that there was minimal signs of *in vivo* toxicities as shown by multiple toxicity indicators [41, 42]. This study has provided the mechanistic insight of the previous observations.

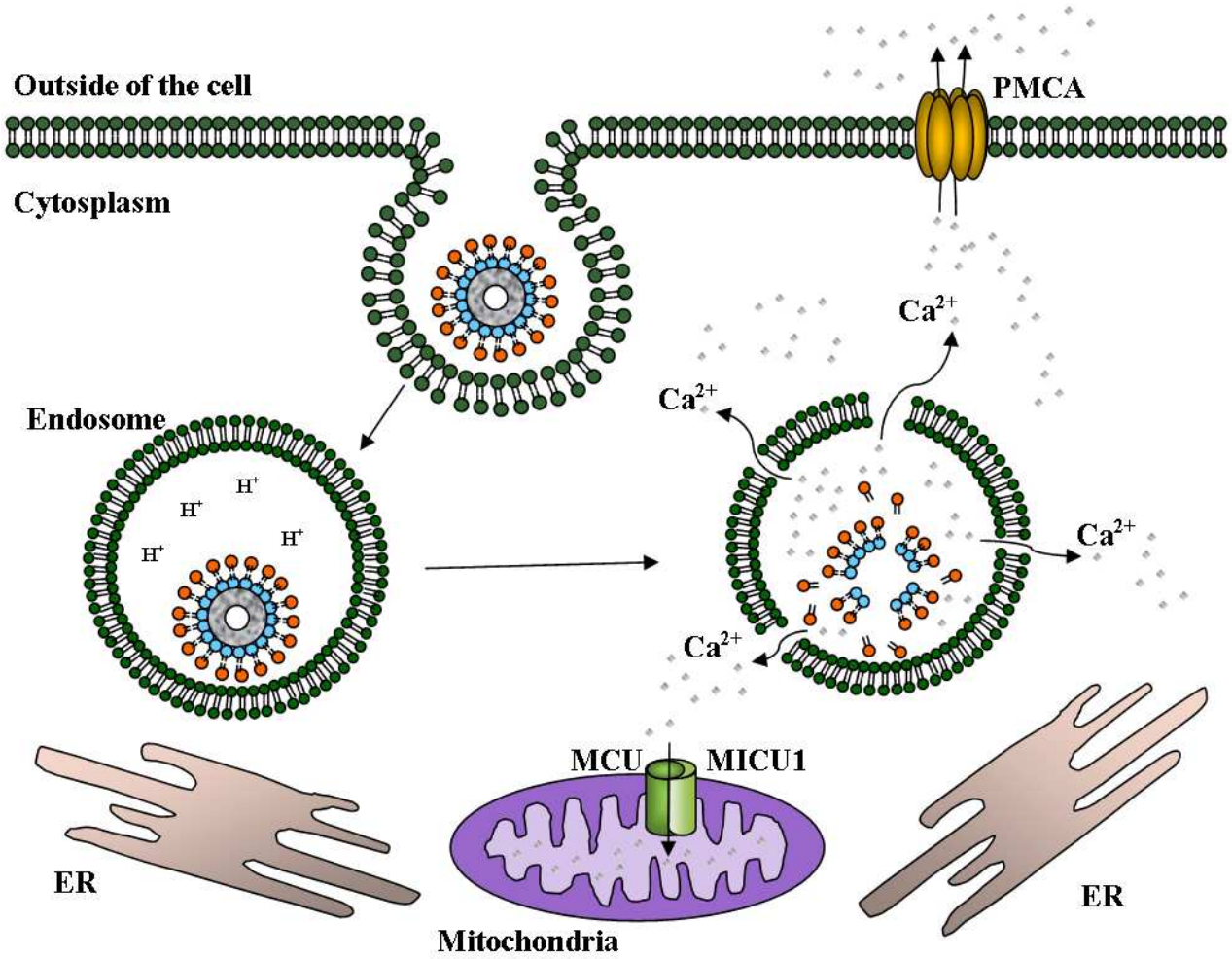

Figure 2.7 Cartoon illustration of the Ca^{2+} removing mechanism after LCP dosing

The elevated cytosolic Ca^{2+} delivered by LCP was quickly managed by PMCA on the plasma membrane and the mitochondrial calcium uniporter (MCU). Mitochondrial calcium-uptake 1 (MICU1) is a calcium sensor, regulates the Ca^{2+}-influx capacity of MCU.

CHAPTER III

SPECT/CT IMAGING AND LCP PHARMACOKINETICS STUDY

3.1 *In vivo* H460 xenograft tumor imaging

Employing all the adjustments made to the procedure to load ^{111}In and improve the washing and coating of the cores, S-LCP NPs coated with DOPC/cholesterol/DSPE-PEG2000 at a ratio of 2/211 were prepared for *in vivo* SPECT/CT imaging of H460 xenograft tumors. S-LCP containing ~0.5 mCi of ^{111}In was injected into the tail vein of mice bearing H460 tumors.

3.1.1 SPECT/CT imaging protocol

All animal work was approved by and performed in accordance with the guidelines of the University of North Carolina Institutional Animal Care and Use Committee. Athymic nude (nu/nu) mice bearing H460 human lung cancer tumors were used. SPECT/CT experiments were performed using a GE eXplore speCZT system. A 7-pin-hole collimator for mice was used to achieve high resolution SPECT imaging. In order to include both the tumor and heart in the same field of view (FOV), 5 x 10^6 or 2 x 10^7 (for the younger tumor model) H460 tumor cells were inoculated subcutaneously on either side of the rib cage.

Each mouse was injected through the tail vein with 200 µL of the final ^{111}In-LCP.

Mice were anesthetized with isoflurane and their body temperature was controlled using a water circuit and warm air. Following injection, the mice were continuously scanned for 2 h to ensure capture of early distribution in blood circulation. Imaging was facilitated through the inoculation of the tumor close to the chest and the reduction of the axial FOV to cover only the chest region. Twelve time points of imaging were acquired during the first 2 h. The mice were scanned at 4, 6, 8, 24, and 26 h post injection.

3.1.2 Results and discussion

After 1.5 h, ^{111}In signals were predominately originated in the blood circulation with some present in the liver and the spleen. Although a clear pattern of accumulation in the tumor was observed before this early time point (Figure 3.1A), the blood content of this organ may contribute significantly to these signals. The blood content of the liver and spleen may have the same effect on the signals in those organs. Both patterns are explained by the fact that the blood was shown to have the highest concentration of ^{111}In. At 4 h, about half of the injected dose was still circulating in the blood (determined by blood samples). Continuous accumulation in the tumor, liver, and spleen was observed as the S-LCP blood concentration decreased (Figure 3.1B). About 27 h after injection, the signal intensity in the blood fell below the average tumor intensity and, consequently, S-LCP tumor accumulation became more apparent (Figure 3.1C).

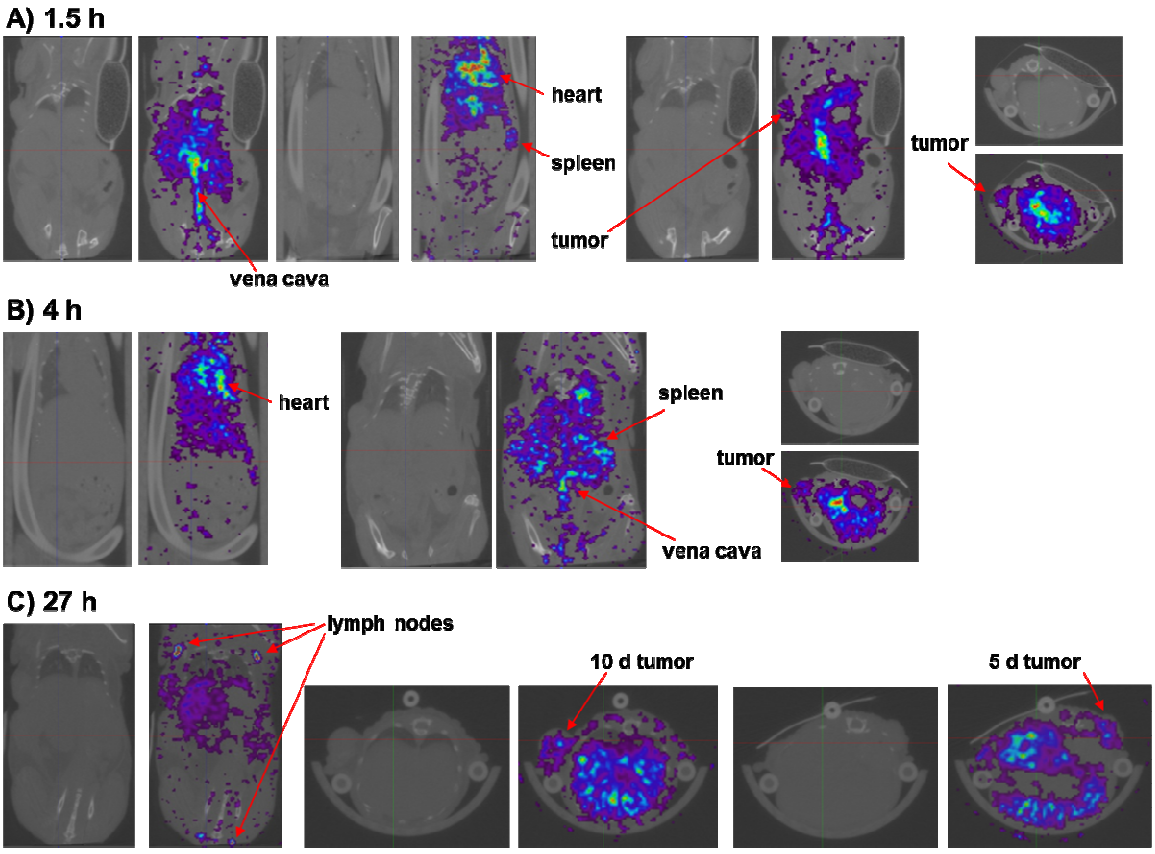

Figure 3.1 SPECT/CT images at three time points post IV injection.

CT images and SPECT/CT overlay images were presented side by side to show anatomical details. Nude mice bearing H460 tumors of two different ages were injected through the tail vein with S-LCP containing ~0.5 mCi ^{111}In. Different horizontal sections and vertical sections were included to show organ images on different section planes.

Unexpectedly, lymph nodes showed the highest accumulation of ^{111}In signal in the SPECT/CT images. Systemic accumulation of NPs in the lymph nodes after IV administration has rarely been reported in previously published literature. Only dextran-coated, ultrasmall super-paramagnetic iron oxide (USPIO) NPs at a size comparable to that of S-LCP had shown similar lymphotropism. These have been evaluated for clinical imaging of lymph node metastasis using MRI after their IV administration [87, 100-104].

However, larger iron oxide NPs coated with dextran similar to or larger than our L-LCP preferentially accumulated in the liver and spleen [87]. Other NPs with similar sizes and PEG grafting exhibited, like our S-LCP, prolonged time in circulation in the blood. However, no preferential accumulation in the lymph nodes was reported [53, 78, 86]. For example, one recent publication reported that PET imaging demonstrated a long-circulating, 15 nm, micellar NP (circulation time longer than S-LCP) that had minimal accumulation in the liver and spleen, with ~6% injected dose per gram tissue (ID/g) tumor accumulation. However, this micellar NP did not exhibit lymphotropism [86]. The authors hypothesized that monomer desorption and cellular internalization and digestion were responsible for the NP clearance. The PET images also indicated that a portion of the ^{64}Cu signal was excreted into the intestine. Another recent publication reported 30 nm Au nanocages for use in PET imaging of tumors also exhibit minimal accumulation in the liver and spleen and no lymphotropism [78]. In this case, rapid and significant clearance of ^{64}Cu signal was observed in the bladder. Therefore, NP lymphotropism may be correlated with NP size and dependent on their surface properties. Coating of the NP surface with a lipid bilayer or dextran may contribute to the unusual lymphotropism. Further studies on LCP lymphotropic behavior will be discussed in Chapter 4.

3.2 LCP pharmacokinetics profile study from both SPECT/CT and organ dissections

3.2.1 PK study from organ dissections

After SPECT/CT imaging, mice were sacrificed and their major organs were collected to determine the biodistribution through gamma counting. Improved S-LCP core washing and outer-leaflet coating methods contributed to the reduction of uptake by

the MPS of ~20% ID/g in the liver and ~13% ID/g in the spleen (Figure 3.2A). This reduced accumulation in the liver and spleen is comparable with many other NPs with similar particle size. For instance, the aforementioned 30 nm Au nanocage showed ~40% ID/g accumulation in the liver and ~30% ID/g in the spleen in a mouse model bearing EMT-6 tumors [78]. A PEGylated, 20 nm gold NP had been reported to achieve ~30% ID/g in the liver and ~15% ID/g in the spleen, which is very close to the levels of S-LCP [53]. The long-circulating, 15 nm micellar NP exhibited the lowest accumulation in the liver and spleen (~4.5% and ~4.6% ID/g, respectively) [86]. However, since the micellar NP was biodegradable and there were ^{64}Cu signals excreted into the intestine, shown in the PET images, it is difficult to ascertain the true levels of accumulation in the liver and spleen in this case.

Organ gamma counting results agreed well with SPECT/CT images indicating around 8% and 13% ID/g tumor accumulation of S-LCP (N=3, $p<0.02$) for two different aged H460 tumors (tumor weight ~0.25 g and ~0.1 g, respectively). Lymph nodes (2 axillary, 2 brachial, 2 inguinal, and 2 popliteal) had the highest accumulations, ~70% ID/g. For the 8 lymph nodes collected, there was ~2.7% ID. This low accumulation in the liver and spleen and high accumulation in the tumor indicates that the performance of this NP is among the best observed to date using radiolabeling quantification methods [53, 78, 86]. After 24 h, over 80% of the total injected ^{111}In dose was retained in the mouse, suggesting elimination of S-LCP from the mouse body was very slow. Thus, the elimination of S-LCP from the blood could be caused by redistribution throughout the body, mainly to the lymphatic system (as shown by the high accumulation in the lymph nodes), and not by excretion from the liver or the kidneys. This hypothesis will be further examined in Chapter 4.

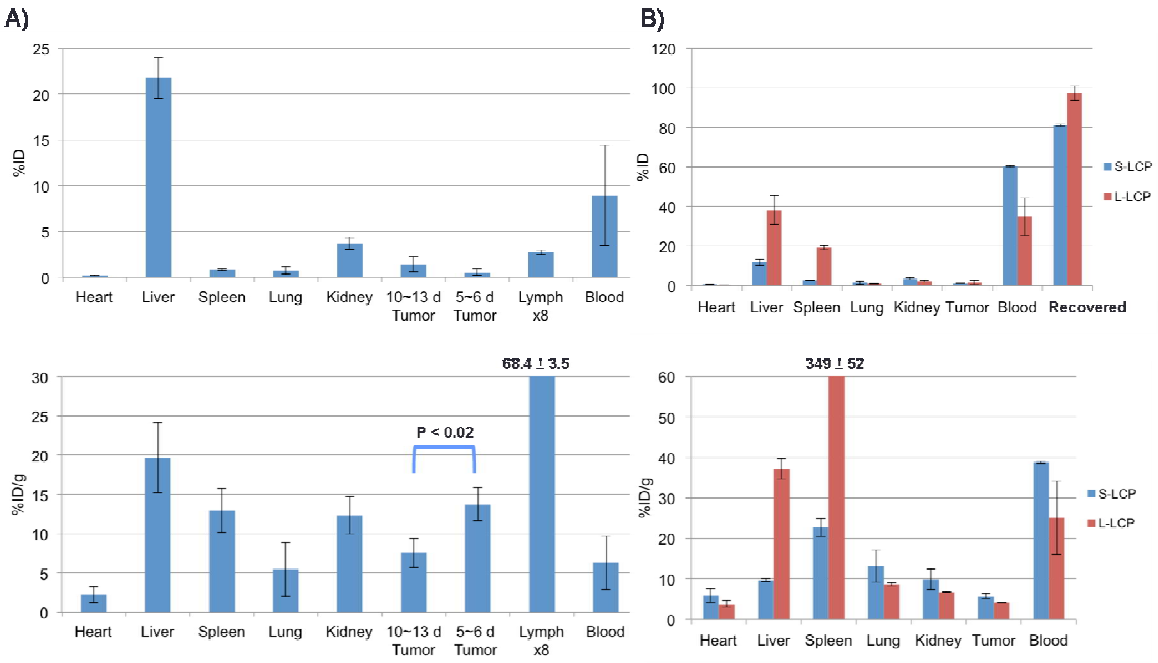

Figure 3.2 LCP biodistribution results from organ dissention

A) S-LCP biodistribution after SPECT/CT imaging. (N=3) B) Biodistribution of S-LCP and L-LCP at 4 h post injection. (N=3)

3.2.2 Compare S-LCP and L-LCP NPs for tumor imaging

To compare whether S- or L-LCP is better for the purpose of tumor imaging, trace amounts of ^{111}In were loaded into both S- and L-LCP and the particles were coated with DOPC/cholesterol/DSPE-PEG2000 at a ratio of 2:2:1. A biodistribution study of these particles was then performed. Figure 3.2B showed the results collected 4 h post IV injection. Tumor accumulation level of L-LCP was slightly lower than S-LCP. However, S-LCP showed better MPS evasion and a higher concentration in the blood.

L-LCP showed slightly lower levels of accumulation in the tumor, but had significantly higher accumulations in the liver and spleen (Figure 3.2B). These results

are consistent with reports on SPIO or gold NPs [53, 87]. Twenty-four hours after administration via tail vein injection, L-LCP also showed lower accumulation in the lymph nodes at 15.6 ± 3.1% (N=3). This pattern could be due to the population of smaller particles generated during the formulation of the L-LCP cores (Figure 2.3A). Because a small amount of uptake by the MPS is preferred in order to avoid toxicity in the liver and spleen and because accumulation of S-LCP was higher than L-LCP in both the tumor and lymph nodes, we conclude that S-LCP is better than L-LCP for the purpose of imaging tumors and lymph nodes.

3.2.3 Validate ^{111}In labeling of LCP NPs with ^{3}H-labeled oligo

To rule out the possibility that ^{111}In encapsulation is not an accurate label for LCP NPs, another biodistribution experiment was completed using S-LCP containing ^{3}H-labeled DNA oligo. The results from the experiment using ^{111}In agreed with those of the study using ^{3}H-labeled oligo, suggesting that labeling LCP cores with either ^{111}In or ^{3}H-labeled oligo accurately represents the biodistribution of S-LCP [105]. However, unlike ^{3}H, which has a low energy beta particle emission, ^{111}In is advantageous for its *in vivo* imaging and real-time NP tracking capabilities.

3.2.4 Pharmacokinetics study from SPECT/CT image analysis

SPECT/CT imaging not only provides *in vivo* biodistribution images of NPs without sacrificing the animal, but also allows the study of pharmacokinetics (PK) of the NPs in multiple organs at various time points in a single animal. Since SPECT/CT imaging has excellent signal linearity (data not shown), quantification analysis could be

performed after the images have been taken. Using AMIDE software, PK profiles of S-LCP NPs loaded with ^{111}In were studied in the blood (using heart as sampling region), tumor, kidneys, and liver (Figure 3.3).

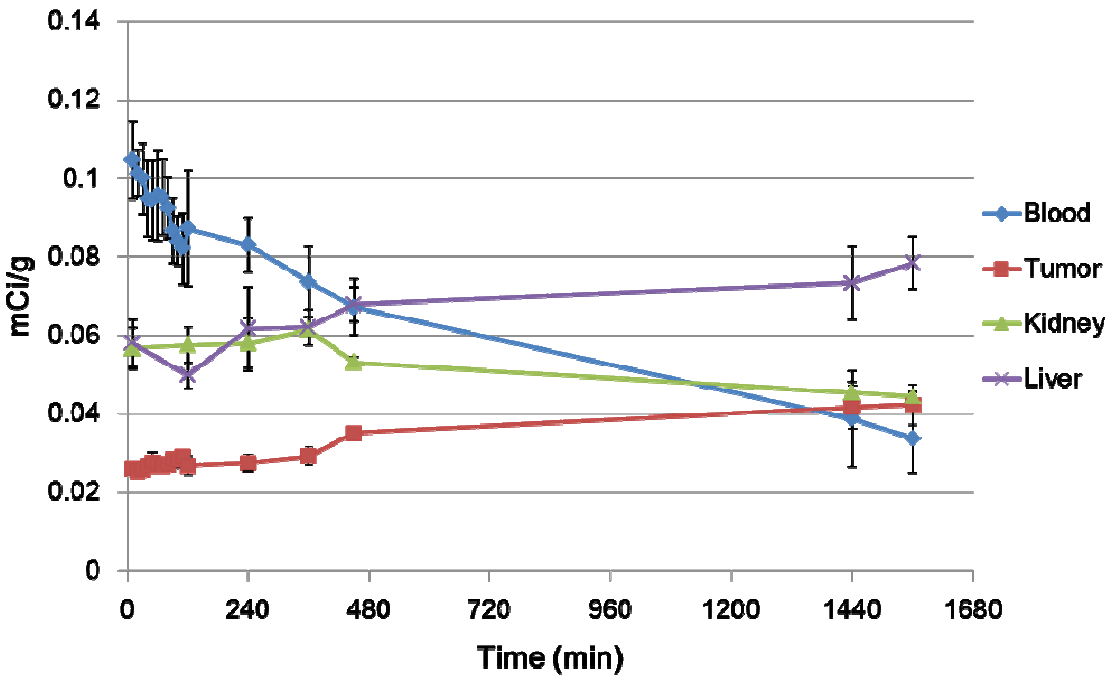

Figure 3.3 PK analysis from the SPECT/CT images using Amide software.

The radioactivity in mCi/g was determined from the SPECT images using Amide software with a standard curve. A) PK trends in the blood indicated a rapid distribution phase in the first 1.5 h (half-life 4.4 h), followed by a slow blood-elimination phase (half-life 18.4 h). B) Tumor had an instant S-LCP accumulation partially explained by the blood content. C) Kidney accumulation could be a combination of rich blood content and a slow accumulation curve which is probably very similar to tumor. D) Liver slowly accumulated S-LCP throughout the scanning period. The instant accumulation had a high contribution by the blood since the liver is a blood-rich organ.

The regions of interests (ROIs) were drawn around the whole heart and the

tumor. Precise contouring along the ventricles was not possible due to imaging resolution and manual drawing limitations. Thus, the method might result in the under-estimation of blood and tumor curves. However, the PK trend in the blood clearly suggested a two-compartment model with a rapid distribution phase within the first 2 h, followed by a slow blood-elimination phase (Figure 3.3). The half-lives of the rapid distribution and slow blood-elimination phases were ~4.4 h and ~18.4 h, respectively. The tumor on the other hand, displayed an initial accumulation of NPs, partially due to blood perfusion and vascular fraction, continued to accumulate. Although there was a significant amount of S-LCP in the blood, the rate of tumor accumulation was determined by the degree of EPR effect in the individual tumors. Prolonged blood circulation of NPs is believed to be the key to enhancing NP tumor accumulation. In our study, however, PK data demonstrated that after a decently long circulation profile was achieved, NP accumulation in the tumor was actually restricted by the tumor-dependent EPR effect. Therefore, reduced MPS uptake and enhanced NP blood circulation are not sufficient for high levels of NP accumulation in the tumor. Additional improvements must be considered.

3.3 Can ligands improve the accumulation level of NP in the tumor?

To determine if the addition of a targeting ligand to S-LCP could enhance the accumulation level of S-LCP in the tumor, the original 20% DSPE-PEG2000 was replaced by 2% DSPE-PEG2000-anisamide (or DSPE-PEG2000-folic acid) mixed with 18% DSPE-PEG2000 in the coating of the S-LCP. Although the biodistribution patterns were altered, the results showed that neither anisamide nor folic acid could improve the accumulation level of S-LCP in the tumor (Figure 3.4A). A recent publication

demonstrated that PEG density above 10% on a nanoemulsion NP may inhibit the function of targeting ligands [106]. When the ligands were conjugated on the distal ends of PEG chains, the increased interactions between the chains, due to the high density of chains, could reduce the ligand's ability to interact with its receptor. To study whether this was the reason why targeting ligands could not improve S-LCP tumor accumulation, the total percentage of DSPE-PEG2000 was decreased from 20% to 10%. The results still indicated that neither ligand could enhance levels of accumulation in the tumor (Figure 3.4B).

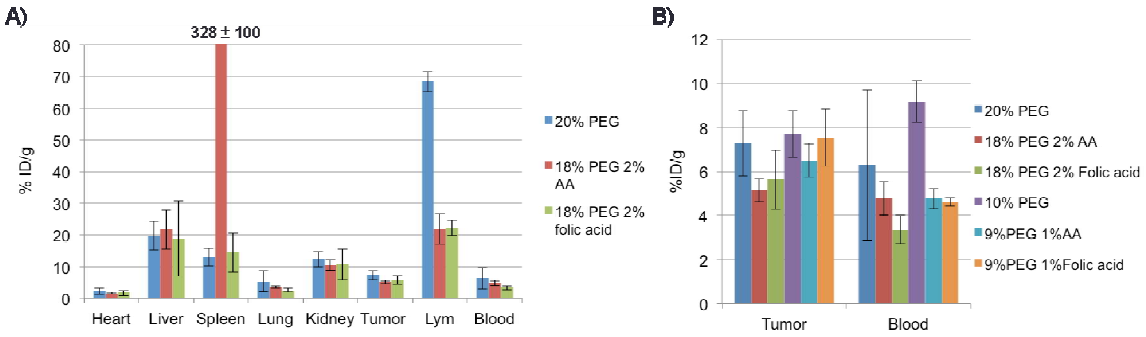

Figure 3.4 Ligand effects on LCP NP biodistribution and tumor accumulation

A) Tumor accumulation and blood retention of S-LCP coated with cholesterol/DOPC and grafted with indicated PEG (and PEG-ligand) contents at 24 h post injection. B) Decrease the total PEG content still cannot enhance accumulation of S-LCP NPs in the tumor. (N=3)

These results support previous reports stating that targeting ligands can improve tumor cell uptake but not total accumulation within the tumor [107, 108], which further suggests that the EPR effect is the rate limiting step in accumulation of NPs. This step in the process occurs before the ligand can enhance uptake of NPs by the tumor cells. On the other hand, strategies such as using metronomic chemotherapy to disrupt tumor

neo-vasculature [109] or vasodilatants [110] to fundamentally enhance the EPR effect have been shown to successfully improve NP accumulation in the tumor

3.4 Tumor age (size) effect on NP accumulation

3.4.1 Tumor blood vessel staining with CD31

In the *in vivo* SPECT/CT and biodistribution experiments we observed that younger tumors tend to accumulate more S-LCP than older ones. We hypothesize that younger tumors might have more disorganized blood vessels, leading to a higher EPR effect. To test the hypothesis, frozen sections for tumors of different ages were prepared and immuno-stained for CD31 (an endothelial cell marker). Fluorescent microscopy images showed that younger tumors exhibited a more disorganized pattern of CD31 staining, suggesting more leaky neo-vasculature (Figure 3.5A). Older tumors had fewer blood vessels that were more organized. Furthermore, tumor cells were more compact in older tumors. Quantification analysis using ImageJ software showed that the number of positively-stained pixels in the younger tumor sections was three-fold higher than that in the older tumor sections (Figure 3.5B).

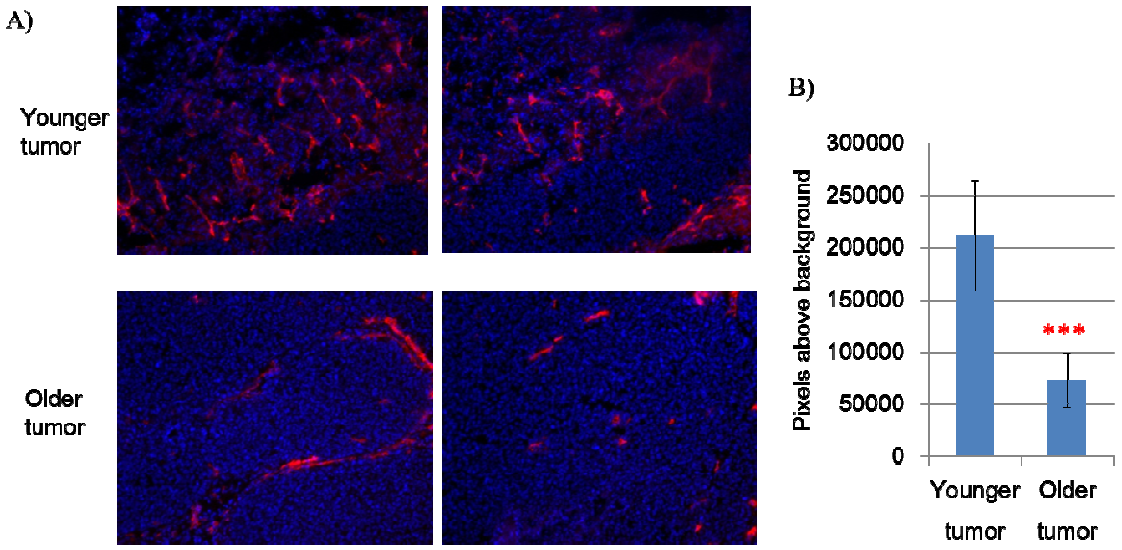

Figure 3.5 Younger tumor had more disorganized blood vessels.

A) Tumor blood vessel stained with CD31-PE. Younger tumor sections (upper two) have more disorganized pattern of staining in the blood vessels compared to the older ones (lower two). B) Quantification analysis using ImageJ software and Student's t-test. (N=7, P<0.0001)

3.4.2 Demonstration of EPR effect with Evans Blue

Next, Evans Blue (purchased from Sigma) was used to demonstrate the EPR effects in both younger and older tumors. Evans Blue binds to serum albumin with high affinity, and has been widely used to quantitatively access the degree of EPR effect in tumor [60], permeability of blood-brain-barrier [111], and peripheral inflammation [112].

Evans Blue was dissolved in PBS at a concentration of 1 mg/mL. Before injection into nude mice bearing two differently aged H460 tumors (younger tumor: 5 days; older tumor: 10 days), the Evans Blue solution was passed through a 0.22 μm filter. Each mouse received 200 μL of Evans Blue through tail vein injection. After 24 h, the mice were sacrificed, and were perfused with 10 mL PBS slowly into the left side of the heart

to remove the blood component of any organ. The tumors were collected and the Evans Blue color in the tumor was visually documented (Figure 3.6A).

The tumors were then weighted and added with 2 mL formamide. The mixture was then incubated at 60℃ and shaken for 48 h to e xtract the Evans Blue. Absorbance at 575 nm was determined using a plate reader (PlateCHAMELEON), and the readings were converted to % ID/g using the standard curve of Evans Blue (Figure 3.6B). As visually demonstrated in Figure 3.6A, younger tumors exhibited a higher degree of Evans Blue accumulation. After quantification, younger tumors had a higher level of accumulation than older tumors (~57% ID/g and ~16% ID/g, respectively). This result supported our hypothesis that younger tumors have more disorganized blood vessels and thus a more pronounced EPR effect. The data support the notion that the EPR effect is the major obstacle to accumulation of particles in the tumor and the degree of the EPR effect is dependent on the age of the tumor being inoculated.

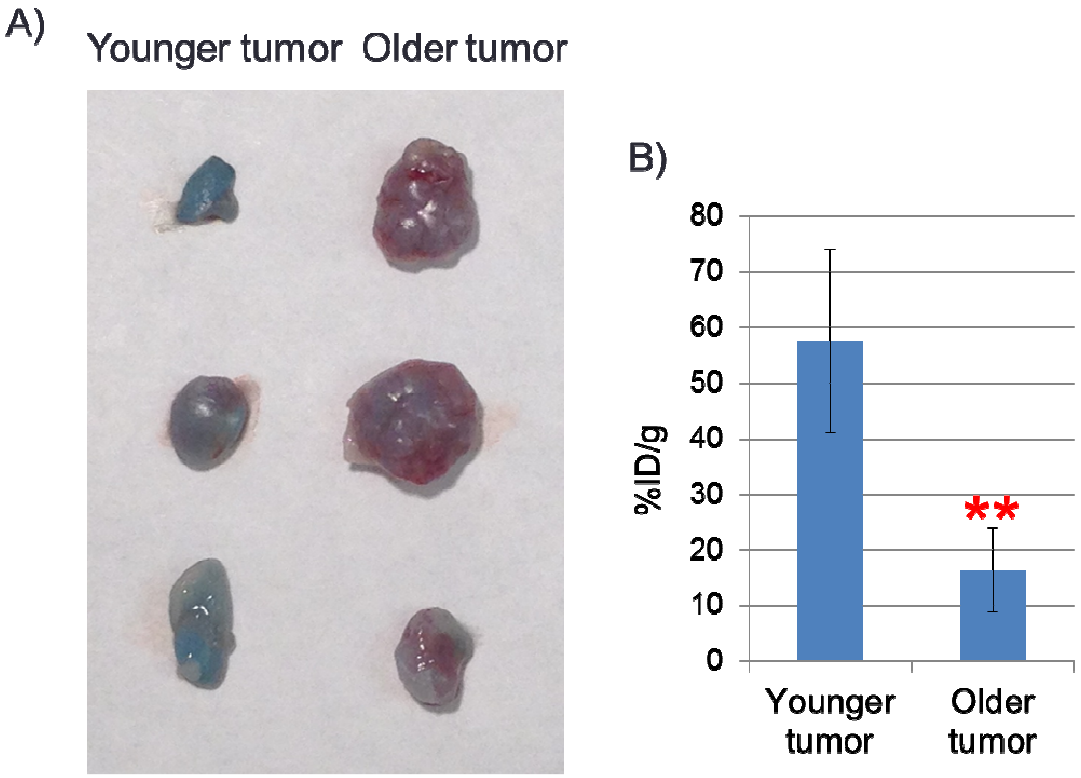

Figure 3.6 Younger tumor had higher EPR effect.

A) Photo of younger and older tumors showing that the younger tumor has higher EPR effect and accumulated Evans Blue at higher level. B) Quantification after extracting Evans Blue from tumor tissue. Absorbance at 575 nm was converted into % ID/g with a standard curve. (N=3, P= 0.017 by Student's t-test)

3.4.3 Discussion

Often times, there is no standard tumor inoculation protocol. The amount of cells required for inoculation varies between cell-lines, and is usually dependent on the growth rate of individual cell-lines. H460 tumors represent a fast growing, xenograft model and usually exhibit significant EPR effects. In this study, the young and old tumors were inoculated with 2×10^7 and 5×10^6 H460 cells, respectively. We observed that by

inoculating more cells, the younger tumor grew at an increased rate, subsequently causing an increased EPR effect and accumulation of NPs. Manipulating the inoculation protocol to work on younger or smaller tumors could potentially result in better imaging or therapeutic outcomes. However, naturally occurring tumor malignancies are usually slow growing and start with a small number of tumor cells. Hence, the question of whether xenografts are valid pre-clinical models for naturally occurring tumors has been raised during the past decade. Genetically engineered mouse models [113, 114] or patient-derived tumor xenografts [115] have provided better, more clinically relevant tumor models and show promise for the future of the field. However, these models still suffer from poor consistency and limited availability [113-115].

3.5 *In vivo* lymph node metastasis imaging with 4T1 model

A variety of human cancers disseminate via regional lymph node metastasis [116]. The ability to image sentinel lymph nodes and evaluate the stage of the metastasis is highly desirable. To demonstrate whether S-LCP can be used to detect lymph node metastasis, a 4T1 murine, breast cancer cell line that expresses both luciferase and green fluorescent protein (4T1-luc2-GFP) was used to establish a lymph node metastasis model [117, 118].

3.5.1 Establishing 4T1 metastasis model

The luciferase and GFP double-expressed 4T1 murine breast cancer cell line (4T1-luc2-GFP Bioware® Ultra Green) was purchased from Caliper. The tumor model was established by hock injection of $2x10^5$ 4T1-Luc2-GFP cells in the right hind leg of 6-

8 weeks old female BALB/c mice [117, 118].

3.5.2 Monitoring 4T1 lymph node metastasis

The luciferase expression allowed tumor and metastasis progress monitoring starting around 10 d after hock inoculation. Bioluminescence imaging was taken using a Kodak In-Vivo FX PRO system within 15 min after intraperitoneal (IP) injection of luciferin at 150 mg luciferin/kg body weight (Caliper).

3.5.3 Imaging lymph node metastasis

After confirming the lymph node metastasis with luciferase imaging (Figure 3.6A), the mice were injected through the tail vein with ^{111}In-S-LCP. SPECT/CT imaging taken at 24 h after injection clearly illustrated the enlarged, tumor-loaded, metastatic lymph node (Figure 3.6B)

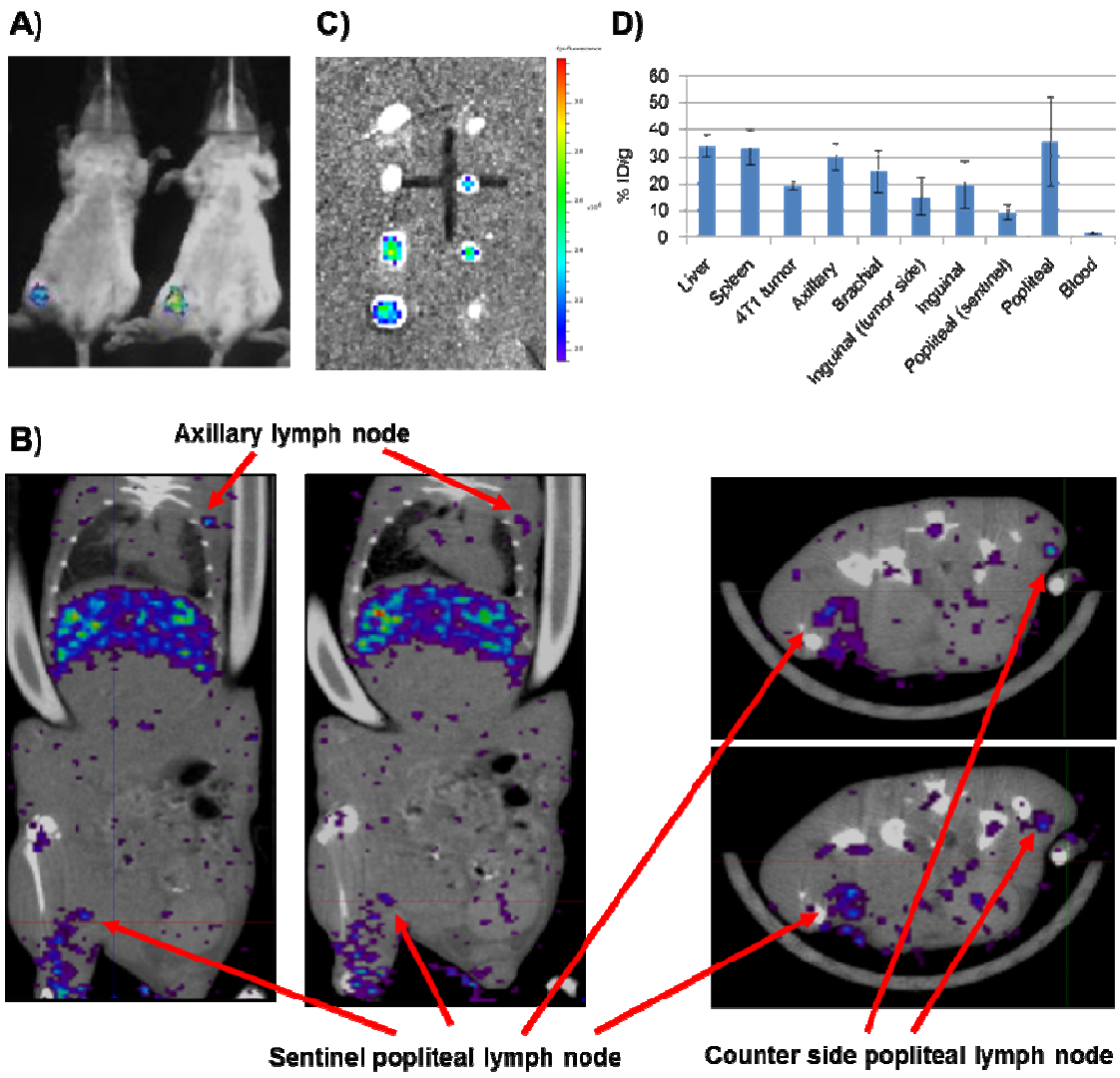

Figure 3.7 Imaging 4T1 lymph node metastasis.

A) Bioluminescence image of two BALB/c mice with strong luciferase activity in their sentinel popliteal lymph nodes. Image was taken 10 d after hock inoculation. B) SPECT/CT images taken 24h post IV injection of ^{111}In loaded S-LCP. Two horizontal and two vertical sections were shown. The size enlarged and tumor loaded sentinel popliteal lymph node was clearly visualized and could be directly compared with the counter side popliteal lymph node. C) GFP fluorescent images of the metastatic 4T1-luc2-GFP cancer cells in the lymph nodes. Eight lymph nodes (from top to bottom: 2 axillary, 2 brachial, 2 inguinal, and 2 popliteal) from both side of one mouse were shown. Sentinel popliteal and inguinal lymph nodes at the bottom left showed the strongest GFP

signals, indicating tumor metastasis. D) S-LCP biodistribution 28h post injection at liver, spleen, 4T1 tumor, and various lymph nodes by gamma counting. (N=3)

An uneven pattern of ^{111}In signal distribution in the metastatic lymph node was probably due to the presence of the tumor mass, an observation that was also reported in other studies [100, 119]. After SPECT/CT imaging, the mouse was sacrificed for GFP imaging of the metastatic cancer in the lymph nodes (Figure 6C) using an IVIS Kinetic imaging system. Organ biodistribution analysis by gamma counting was also conducted to confirm the SPECT/CT imaging results (Figure 6D).

3.5.4 Discussion

The total accumulated dose in the metastatic lymph nodes was ~1.5 times higher than that in the counter-side, popliteal lymph nodes. Due to enlargement of the metastatic lymph nodes caused by tumor growth and inflammation, the accumulation level was reduced to ~9.1% ID/g as a result of increased organ weight of the metastatic lymph nodes, whereas the counter-side, popliteal lymph node achieved 35.4% ID/g. However, the accumulated ^{111}In signal was sufficient for imaging, leading to the observation of the uneven distribution pattern [119]. The overall lymph node accumulation level in this BALB/c, 4T1 model was lower than what was observed in the C57BL/6 and nude mice. The decrease could be attributed to higher MPS function induced by the 4T1 tumor, as indicated by a significantly larger spleen in this model (data not shown). However, the 4T1 tumor achieved high accumulation in the tumor (19.1% ID/g), which might also contribute to the overall lower accumulation in the lymph nodes of this model. This work demonstrates the feasibility of using ^{111}In loaded S-LCP to image metastatic lymph nodes via intravenous injection.

CHAPTER IV

LCP LYMPHOTROPISM STUDY

4.1 Introduction

The lymphatic system is a central component of the immune system and serves as the secondary circulation system responsible for the drainage of fluid from the extracellular space, proteins, and waste products into the blood. Lymph nodes also play an important role in diseases such as infection, inflammation, and cancer [120]. Primary tumors usually begin metastasis by invading the sentinel lymph nodes, which then serve as a reservoir for further spread of cancer cells [121-123].

The delivery of genes and drugs to both the local, draining lymph nodes and the lymphatic system as a whole is a challenging task. Certain lipophilic compounds such as long-chain fatty acids, cholesterol esters, triglycerides, and lipid-soluble vitamins can be transported through the lymphatic channels [120, 124]. However, most chemotherapy agents cannot gain access to the lymphatic system after conventional IV infusion, including the lymph node metastasis [120, 124]. Consequently, the development of clinical treatments of lymph node metastasis and other cancers has remained elusive.

Many different types of NP, including liposomes, silica NPs, and other polymer-based drug delivery systems, have exhibited improved efficiency in regionally delivering drugs to the lymphatic system [125-129]. For example, IP injected liposomes containing doxorubicin result in an 8- to 14-fold (4 h post injection) and a 3- to 6-fold (24 h post

injection) increase in doxorubicin concentration in the draining lymph nodes in rats compared to the increase caused by free doxorubicin [125]. However, no significant difference was observed after IV administration. Thus, effective delivery by IV administration to the lymphatic system allowing the detection of lymph node metastasis is still in demand.

LCP NPs were first developed for siRNA delivery [40-42] and have recently been successful in delivering gemcitabine mono-phosphate (Zheng et al, manuscript in submission). Successful loading of ^{111}In into LCP NPs has also been demonstrated in Chapter 3 for SPECT/CT imaging and PK/biodistribution studies. In the SPECT/CT imaging study, an accumulation level as high as ~70% ID/g in lymph nodes throughout the body was observed following IV injection. That ^{111}In can form precipitate with phosphate in a manner very similar to calcium is the principle behind ^{111}In loading and entrapment in the LCP core. Taking advantage of the Ca-P core formation principle, a variety of anti-viral nucleoside analogue drugs [82-85] could be entrapped via a similar strategy as gemcitabine mono-phosphate. This property of the LCP, along with its lymphotropism, allows the use of the NP formulation for the delivery of nucleoside-analog drugs for the treatment of diseases such as metastasis and HIV infection in the lymph nodes.

The uniquely strong lymphotrophism of the LCP after intravenous administration could present great potential for the development of lymphatic metastasis and viral infection therapies. Thus, the studies on the lymphotropism of LCPs of different sizes using several administration techniques may provide further insight into future designs of systems for the delivery of drugs to the lymphatic system.

4.2 Accumulation of S-LCP in the lymph nodes

As was demonstrated in Chapter 3, S-LCP with an outer-leaflet coating of DOPC/Cholesterol/DSPE-PEG_{2000} (2:2:1) had little accumulation via MPS in both the liver and spleen. The particle did, however, accumulate at a level of 8% ID/g or higher in H460, subcutaneous tumor and 4T1 metastasis models (Chapter 3.2 & 3.5). Furthermore, lymph node accumulation as high as ~70% ID/g was observed (Figure 4.1).

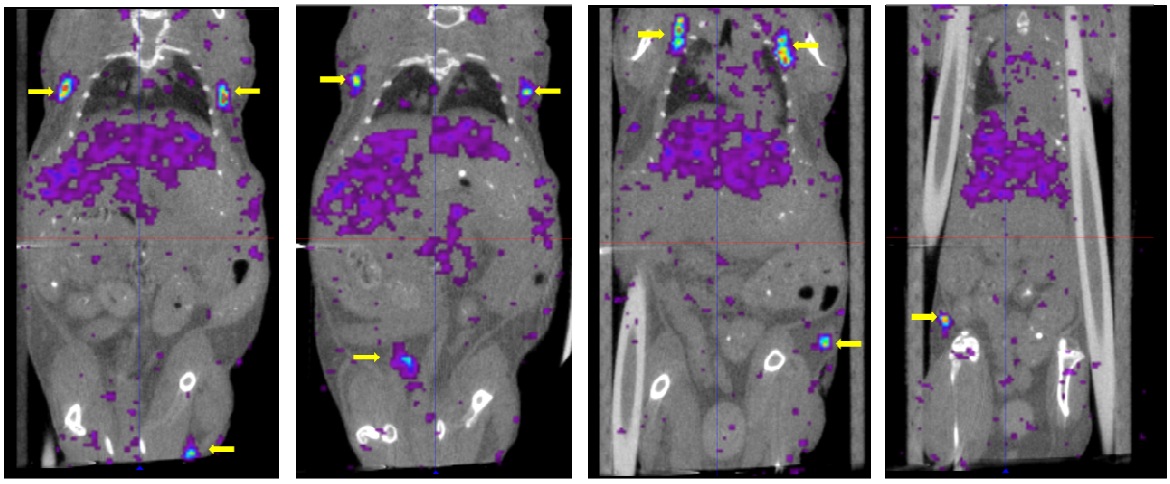

Figure 4.1 Accumulation of S-LCP-DOPC with 20% PEGylation in the lymph nodes of nude mice.

Yellow arrows indicated high accumulation level at ~70% ID/g in the symmetrical lymph nodes. Four different SPECT/CT sections were presented. SPECT/CT images were taken at 27 h post IV injection.

In order to make sure this lymph node accumulation is not unique to tumor-bearing nude mice, a similar SPECT/CT imaging experiment was performed on wild type C57BL/6 mice. As shown in Figure 4.2, symmetrical lymph nodes throughout the animal

were observed to accumulate significant amounts of In-111 loaded S-LCP-DOPC with 20% PEGylation. This confirmed that the lymphotropism of S-LCP NPs also existed in normal and healthy mice.

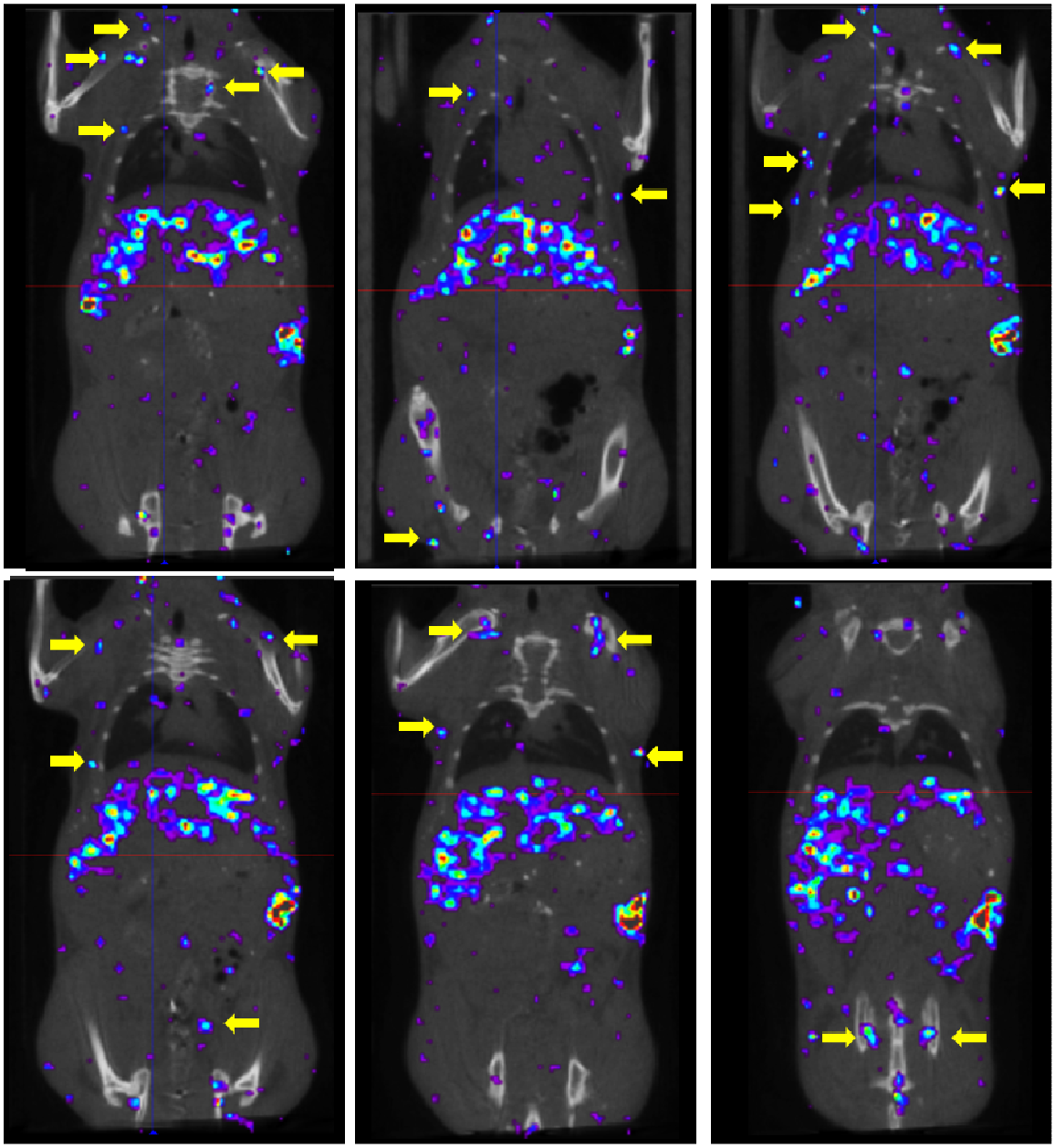

Figure 4.2 Accumulation of S-LCP-DOPC with 20% PEGylation in the lymph nodes of C57BL/6 mice.

Six different SPECT/CT images taken at 24 h post IV injection were included to show that

symmetrical lymph nodes (yellow arrows) throughout the body accumulated significant amount of S-LCP.

4.3 Hypothesis for LCP NP lymphotropism

When coating S-LCP NP with DOTAP/Cholesterol/DSPE-PEG_{2000} (2:2:1), accumulation of the particles in the hepatocytes of the liver was high and uptake by the Kupffer cells was low (Liu et al, manuscript in submission). This efficient delivery to the hepatocytes could be partly attributed to the small particle size of S-LCP NPs, which allows them access to the fenestrated endothelial cells of the liver and encourages hepatocyte targeting mediated by apolipoprotein-E [130].

^{111}In gamma counting indicated that 24 h after injection, the mice retained ~85% of the injected dose. However, when all major organs (heart, liver, spleen, lung, kidney, and 8 lymph nodes) were collected and measured, only ~45% of the injected dose was recovered (Figure 3.2A). Furthermore, SPECT/CT imaging confirmed that there was no significant excretion of the particles from the bodies of the mice during the experiment (Figure 3.1 & 4.1).

Our findings led to the hypothesis that S-LCP-DOPC with 20% PEGylation could penetrate tissues, enter the lymphatic system, and accumulate in the lymph nodes efficiently due to (1) small size (~25 nm), (2) a well-PEGylated, lipid surface, and (3) a slightly negative surface charge. The accumulation of the nanoparticles in the lymphatic system can also explain the reduction in blood concentration while maintaining minimal excretion and organ accumulation (liver, spleen, etc., Figure 3.3).

4.4 S-LCP NPs was more tissue penetrating

4.4.1 Experimental design

Due to the difficulty of directly observing particles penetrating into tissues from circulation, we designed an intramuscular (IM) injection experiment comparing S- (~25 nm in diameter) and L-LCP (~67 nm in diameter) NPs with or without a coating of 20% PEG in the outer leaflet to test our hypothesis. The NPs were IM injected to the right hind leg of C57BL/6 mice. The volume of the injection was limited to 10μL to reduce tissue damage. After 3 or 24 h, the mice were sacrificed and major organs, including lymph nodes and the injected leg, were collected for gamma counting. Draining popliteal lymph nodes were collected and 4 counter-side, distal lymph nodes (1 axillary, 1 brachial, 1 inguinal, and 1 popliteal from the counter side of the IM injection) were also collected for comparison. The gamma reading was corrected for the ^{111}In decay factor during analysis. Statistical analysis was performed using a Student's t-test. Our hypothesis was that if S-LCP NPs have the ability to achieve high tissue penetration following local intramuscular injection, they can move more freely in the tissue, enter into circulation in the blood, and accumulate in the distal lymph nodes.

4.4.2 Results and discussions

When the NPs were PEGylated, both S-and L-LCP NPs had an early blood distribution (observed at 3 h) that could be explained by the mechanical force created by the injection (Figure 4.3). In support of our hypothesis, S-LCP NPs exhibited much higher tissue penetration between 3 and 24 h than L-LCP NPs, as illustrated by decreased retention at the injection site ($P< 0.01$, $N=3$) and a sustained concentration in

the circulation. Although there was some accumulation of S-LCP NPs in the liver, the S-LCP NP depot at the IM injection site served as a reservoir to provide a continuous supply of NPs to the blood. Distal lymph nodes were able to accumulate ~41% ID/g of IM injected S-LCP NPs.

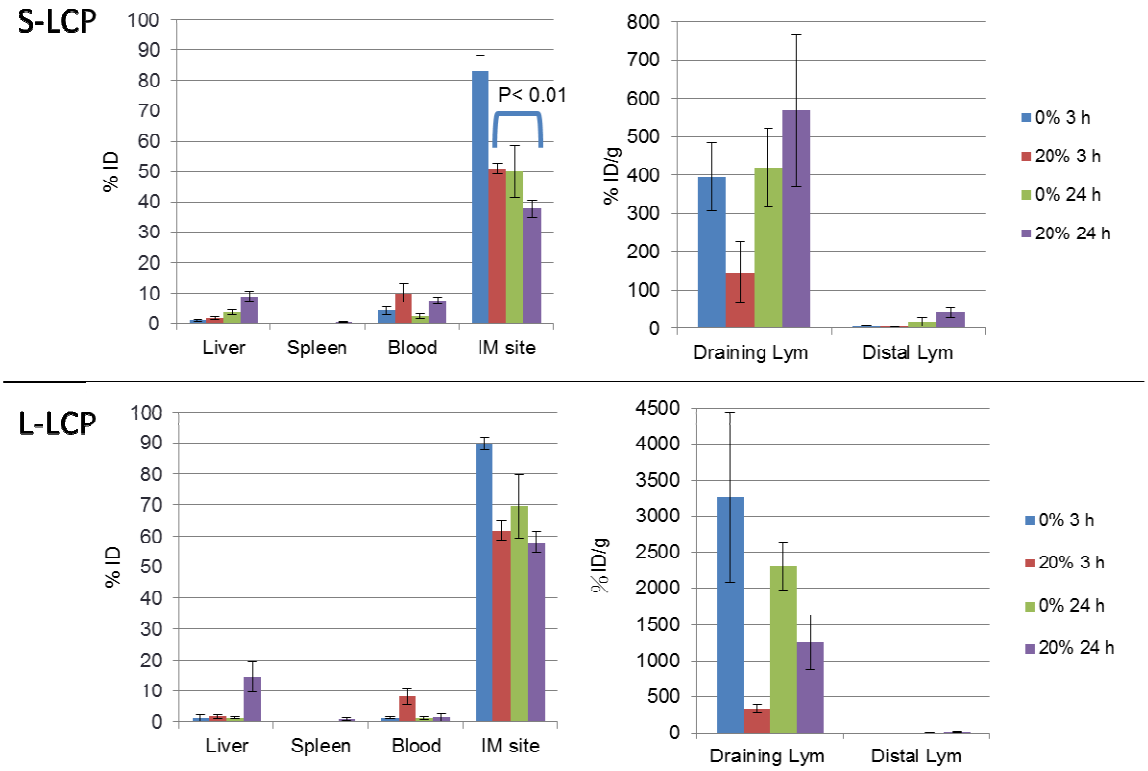

Figure 4.3 IM injection experiments showing that S-LCP NPs is more tissue penetrating than L-LCP NPs

Biodistribution comparison after IM injection of ^{111}In loaded S- and L-LCP coated with or without 20% DSPE-PEG$_{2000}$. Mice were sacrificed at 3 h or 24 h post IM injection.

As the initial blood distribution of PEGylated, L-LCP was cleared by the liver, the L-LCP depot at the IM injection site could not penetrate into the blood to maintain the NP concentration. The L-LCP depot was limited to the injection site and did not decrease significantly between 3 and 24 h post-injection (Figure 4.3). The larger NPs were favored

by the MPS uptake processes; PEGylation in a manner similar to that of the smaller NPs did not alter this pattern [53, 78]. This phenomenon may explain why PEGylated, L-LCP NPs accumulate in the draining lymph node more than S-LCP NPs. In either case, however, the effects of PEG protection in reducing their uptake by the MPS (i.e., local macrophages and dendritic cells) were clear.

Without PEGylation, both S- and L-LCP NPs had limited mobility (though S-LCP NPs were still more mobile), trapping more than 80% of the injected dose at the site of injection after 3 h. Since there was no PEG protection against MPS, rapid and efficient phagocytic uptake lead to high accumulation in the draining lymph nodes at both 3 and 24 h post-injection. Larger particles without PEGylation were preferentially taken up by the MPS, as demonstrated by their accumulation levels of ~3000% ID/g in the draining lymph nodes after 3 h.

4.5 Different distribution pattern of S-LCP and L-LCP in the draining lymph node

Since S-LCP was more active to penetrate tissues and was only minimally taken up by the MPS due to their smaller size, one reasonable prediction is that the majority of S-LCP was drained into the lymph nodes as individual particles. On the other hand, the majority of efficient accumulation of L-LCP in the lymph nodes after IM injection is most likely MPS mediated [131]. To confirm this prediction, S- and L-LCP, both with 20% PEGylation and loaded with Texas-Red labeled DNA oligo, were used to repeat the IM injection experiment.

4.5.1 Experimental design

Double-stranded oligo DNA (synthesized by Sigma, Texas-Red was labeled on the sense strand, sequence: 5'-TxRd-CAAGGGACTGGAAGGCTGGG-3') was added to the calcium emulsion during the preparation of the LCP cores. Followed by the same core preparation and outer leaflet coating methods with or without 20% DSPE-PEG_{2000}, 10 μL IM injection of this Texas-Red oligo loaded LCP NPs were used for the experiment examining the distribution in the draining lymph nodes.

After 24 h, the draining lymph nodes were collected and fixed with formalin for frozen section and observation under confocal microscopy. The lymph nodes were fixed in formalin overnight then put in 30% sucrose solution for another overnight to help preserve the morphology of the tissue. The lymph nodes were then mounted in OCT (optimum cutting temperature) compound and snap-frozen using liquid nitrogen. Frozen sections were cryosectioned at a thickness of 20 μm. FITC labeled antibodies against CD11c or CD11b were diluted to a concentration of 1:500 for immunostaining. After wash with phosphate-buffered saline, the slides were mounted with DAPI containing mounting medium for confocal microscopy observation using a Leica SP2 confocal microscope.

4.5.2 Results and discussions

As shown in Figure 4.4, labeled S-LCP was rarely overlapped with CD11c (dendritic cell marker) or CD11b (macrophage marker) staining. Since dendritic cells and macrophages were the two major phagocytic cells in the lymph nodes, our results suggested that S-LCP remained as individual particles in the lymph nodes. In the case of

L-LCP, Texas-Red fluorescence was mostly overlapped with CD11c and partially overlapped with CD11b. Combined with the observation that IV injected L-LCP had low accumulation in the lymph nodes, this result suggested that after IM injection, L-LCP accumulation in the draining lymph nodes was mainly mediated by uptake by MPS at the injection site, after which the MPS cells migrated to the draining lymph nodes.

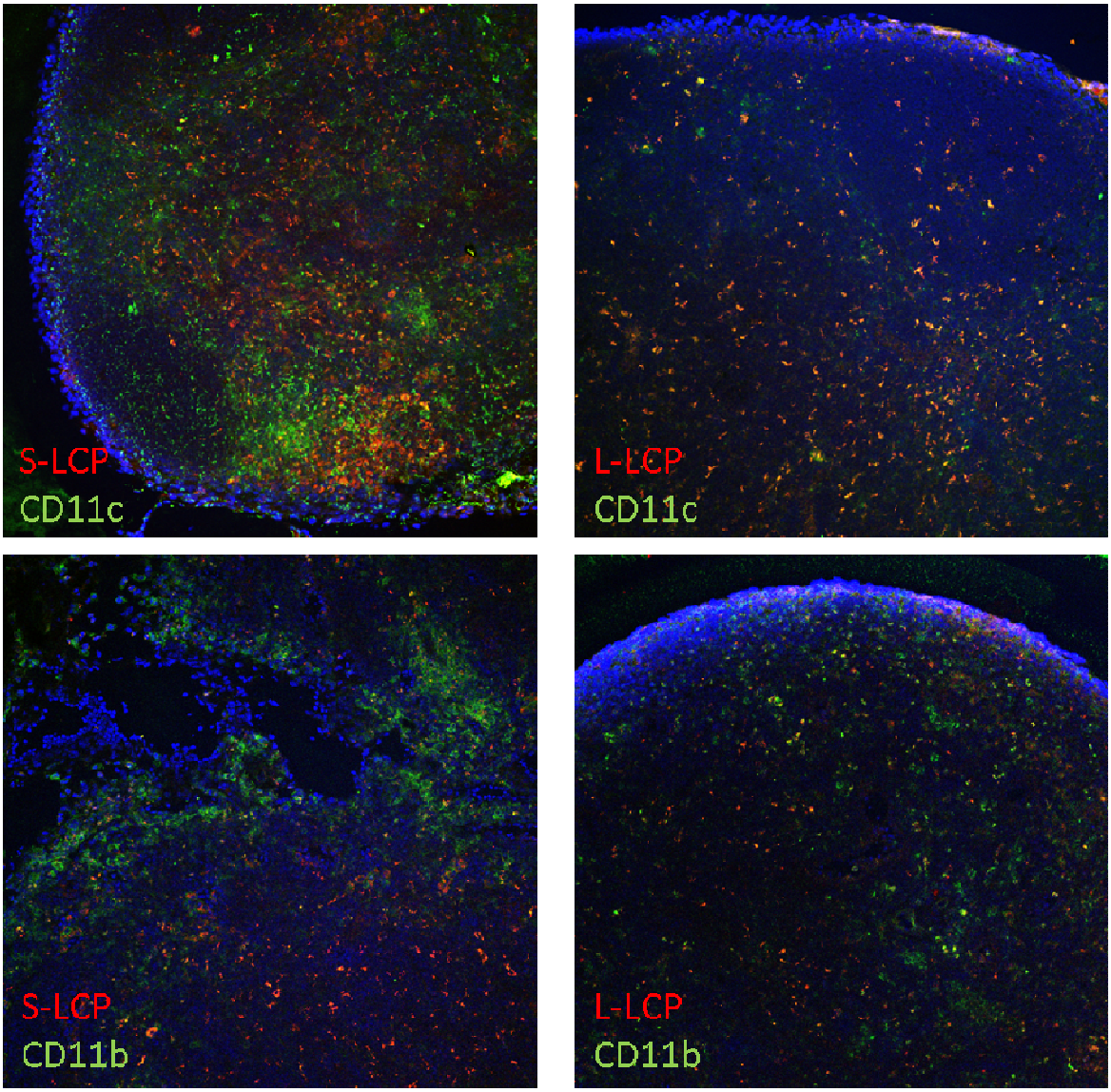

Figure 4.4 Different biodistribution patterns of S- and L-LCP NPs in the lymph nodes

Co-localization of LCP with phagocytic cells in the draining lymph node observed with confocal microscopy. LCP was labeled with Texas-red-labeled oligo and phagocytic cells (CD11c for

dendritic cells and CD11b for macrophages) were labeled with green. Left panels are for S- and right panels are for L-LCP, respectively.

4.6 PEG coating for S- and L-LCP

To demonstrate the importance of PEGylation to the lymphotropism of S-LCP, an experiment varying the amount of PEG coating on the S- and L-LCP was conducted. Geometrically, NPs will have increased curvature as the NPs become smaller. In order to provide a comparable degree of surface protection, a higher degree of PEGylation would be required by an S-LCP (~25 nm) than an L-LCP (~67 nm). However, smaller NPs might inherently possess a stealth property that allows them to avoid uptake by the MPS and thus require less PEGylation. In order to address this apparently contradictory question, the *in vivo* biodistribution of S- and L-LCP-DOPC loaded with ^{111}In and coated with either 0%, 5%, 10%, or 20% DSPE-PEG_{2000} was studied following IV injection.

S-LCP-DOPC NPs without PEGylation exhibited high accumulation in the liver and spleen, as predicted. However, there was no difference observed among groups modified with 5, 10, and 20% PEG, indicating that S-LCP-DOPC do not require a high degree of PEGylation (Figure 4.5A). As little as 5% PEG reduced MPS accumulation and increased lymphotropism at levels comparable to NPs with 20% PEGylation. On the other hand, increased PEGylation on L-LCP-DOPC was beneficial, as liver accumulation of the NPs decreased with increasing amounts of PEGylation (Figure 4.5B). When coated with 5% PEG, the accumulation of L-LCP became higher in the spleen compared to NPs without PEG. Increasing the amount of PEG to 10 or 20% can further reduce accumulation of the particles in the liver, but accumulation in the spleen remains unchanged. This observation suggested that PEGylation could significantly reduce

uptake by the MPS in the liver, while the spleen seemed to be very sensitive to the size of NPs. Only when the NP size was reduced, could we achieve significant reduction in the amount of accumulation of the NPs in the spleen. This accumulation pattern holds true for many other types of NPs in addition to the one described here [53, 78].

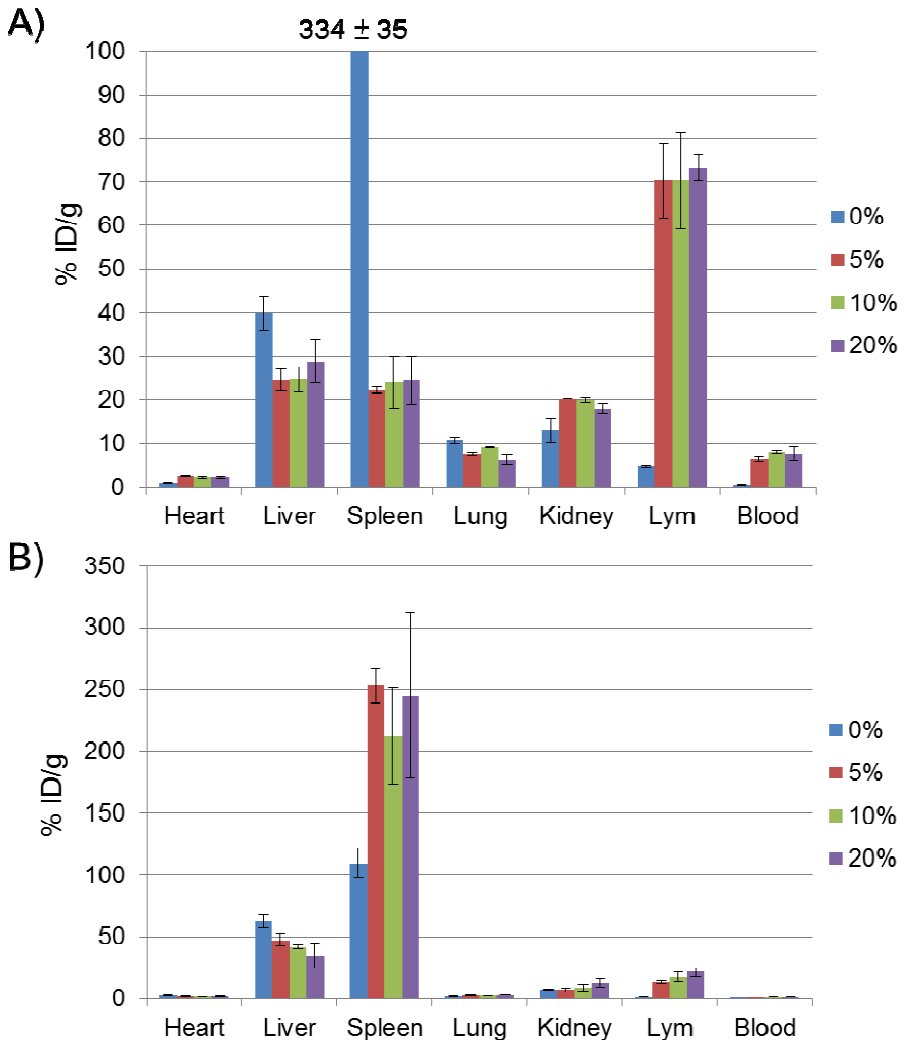

Figure 4.5 Evaluation of the effect of PEGylation on S- and L-LCP-DOPC NPs.

Effect of PEGylation on the biodistribution of S-LCP (A) and L-LCP (B) with different degree of PEGylation at 0%, 5%, 10%, and 20% were shown.

Even when PEGylated at 20% PEG, L-LCP exhibited much lower accumulation in the lymph nodes compared to S-LCP NPs (~21% vs 70% ID/g, respectively). The lower degree of accumulation in the lymph nodes could be explained by the population of smaller particles that was generated as a by-product during the process to create the L-LCP cores (Figure 2.3A). Alternatively, NPs could be carried by MPS cells in the periphery and migrated into the lymph nodes [131].

4.7 Intraperitoneal injection of LCP NPs

Whether LCP NPs could be administered via IP injection was also evaluated. As shown in Figure 4.6A, IP injection of S- or L-LCP-DOPC with 20% PEGylation resulted in biodistribution profiles similar to those observed after IV injection. The IP injected LCP NPs were also able to gain access to blood circulation efficiently. The accumulation of the particles in the liver, spleen, and lymph nodes was only slightly lower when administering particles via IP injection compared to administration via IV injections.

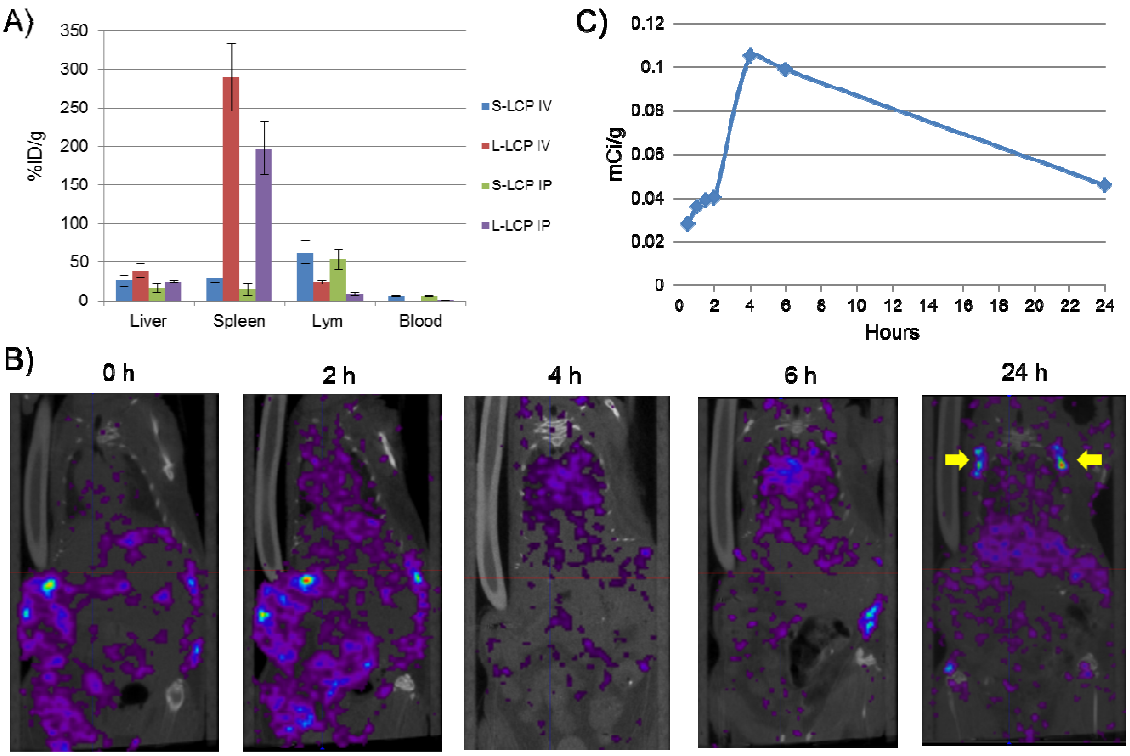

Figure 4.6 Administering LCP NPs by IP injection

A) IP injection of both S- and L-LCP-DOPC with 20% PEGylation led to very similar biodistribution result as IV injection. B) SPECT/CT images showing that the IP injected S-LCP-DOPC with 20% PEGylation could be fully absorbed into circulation in the blood and result in similar accumulation in the lymph nodes at 24 h (yellow arrows). C) Blood PK profile analyzed from SPECT/CT images by AMIDE software using heart as reference.

To further confirm this result, a SPECT/CT imaging experiment with IP injected ^{111}In loaded, S-LCP-DOPC with 20% PEGylation was conducted (Figure 4.6B). As the SPECT/CT images indicated, S-LCP was located in the peritoneal cavity directly following IP injection. In the image taken at 2 h, it was clear that a portion of S-LCP gain access into the blood circulation, as illustrated by the ^{111}In signals in the heart. Note that, due to the mice being anesthetized during the first 2 h, the absorption of S-LCP into the blood stream might be delayed. From images taken at 4 and 6 h, we determined that the absorption of S-LCP into the blood was almost complete at that time point. The

SPECT/CT images were almost identical to those taken after IV injection. At 24 h post IP injection, accumulation of S-LCP in the lymph nodes was also similar to that seen in mice treated with IV injections (Figure 4.1).

Figure 4.6C showed the blood PK curve acquired from SPECT/CT image analysis. The blood concentration trends after 4 h in mice treated with IP injections were almost identical to those in mice treated with IV injections (Figure 3.3). The PK properties of S-LCP after peritoneal absorption are essentially the same as those of IV injected NPs, suggesting S-LCP NPs gain access to the blood stream as un-modified, individual NPs.

4.7.1 Discussions

The exact mechanism of S- and L-LCP absorption in the peritoneal cavity to the blood circulation is not fully known. The surface charge of NPs has great impact on the peritoneal absorption ability of NPs [132, 133]. Neutral or zwitterionic gold NPs have been shown to enter circulation rapidly after IP injection. However, gold NPs with both a strongly positive or strongly negative charge exhibit a limited ability to enter the blood stream [132]. The S-LCP-DOPC with 20% PEGylation possessed a slight negative charge (~-20mV, Table 2.3). This result suggests an alternative route for LCP NP administration.

4.8 *In vivo* lymph node gene delivery with LCP NPs

The ability of S-LCP to deliver genes to the lymph nodes was demonstrated using a plasmid containing RFP cDNA. An oligo-arginine peptide flanked by two

cysteines (sequence: CR8C) that significantly enhances the gene-expression level in a study of LCP mediated delivery of genes to hepatocytes was also used (Hu et al., manuscript in submission). S-LCP loaded with the RFP plasmid, CR8C peptide, and ^{111}In were prepared for this study. The cationic lipid, DOTAP, was included in this study for outer leaflet coating to compare with DOPC since DOTAP was known for its higher transfection activity. PEGylation at 20% was still used for both DOTAP and DOPC coated S-LCP NPs.

4.8.1 Experimental design

S-LCP cores were loaded with RFP plasmid and CR8C peptide (synthesized by Peptide 2.0 Inc.) by mixing 50 μg RFP plasmid and 50 μg CR8C peptide sequentially with 50 μL of 500 mM $CaCl_2$ solution with some $^{111}InCl_3$ for biodistribution evaluation. The core preparation and coating with an outer leaflet were completed following the same procedure described in Chapter 2. Outer leaflet lipids of 40% DOPC (or DOTAP) plus 40% cholesterol and 20% DSPE-PEG_{2000} were used for coating. Each C57BL/6 mouse received 200 μL of the final S-LCP with 20% PEGylation containing 10 μg of RFP plasmid and 10 μg of CR8C peptide by IV injection. After 24 h, the mice were sacrificed and major organs, including 8 lymph nodes, were collected for RFP fluorescence imaging using a Carestream In-Vivo Imaging System FX Pro and gamma counting.

4.8.2 Results and discussions

As demonstrated in Figure 4.7A, S-LCP-DOTAP with 20% PEGylation had high accumulation in the liver (explained mainly by uptake by hepatocytes but not Kupffer cells; Liu et al, manuscript in submission), but ^{111}In gamma counting indicated much

lower accumulation in the lymph nodes. On the other hand, S-LCP-DOPC with 20% PEGylation showed accumulation that was low in the liver and spleen, but high in the lymph nodes. The RFP liver gene expression level was also high in the mice injected with S-LCP-DOTAP with 20% PEGylation, which correlated well with the accumulation level (Figure 4.7B).

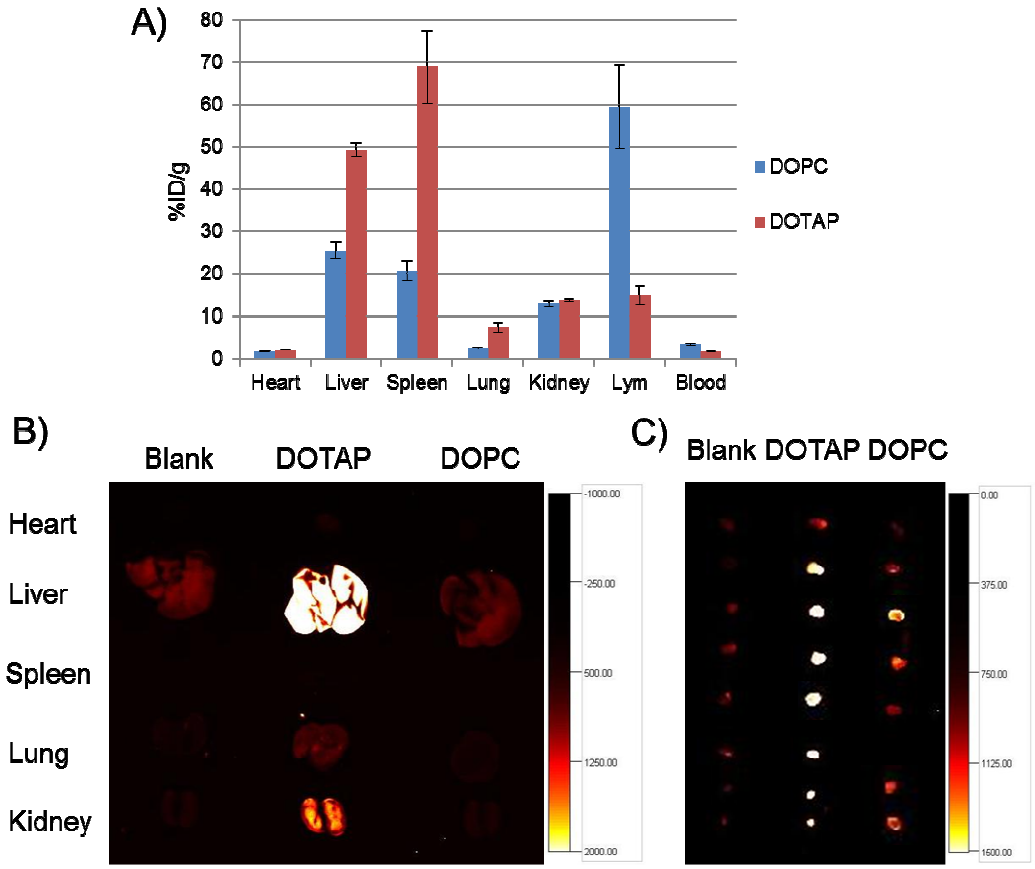

Figure 4.7 Gene delivery to the lymph node by IV injection

A) Biodistributions of S-LCP-DOPC and S-LCP-DOTAP with 20% PEGylation at 24 h post IV injection determined by gamma counting. RFP gene expression at the major organs (B) and the eight lymph nodes (C) were shown by RFP fluorescent imaging.

For RFP gene expression in the lymph nodes, although S-LCP-DOPC had higher accumulation in the lymph nodes, the RFP expression level was lower than that produced by injection with S-LCP-DOTAP (Figure 4.7C). There are two possibilities to explain the observation. The first is dependent on the fact that positively charged DOTAP is known for its high transfection activity, due to its ability to facilitate the endosome escape. The higher expression of RFP despite the lower delivered dose suggested that S-LCP-DOTAP probably exhibited a higher gene expression activity than S-LCP-DOPC. Alternatively, positively charged DOTAP could also aid in the cellular uptake process after PEG shedding [134, 135]. Bioavailability of S-LCP-DOPC might be limited by cellular uptake in the lymph nodes; if cellular uptake is low, bioavailability of the particles is likely to be low as well (Figure 4.4).

However, a DOPC coating still provides specific accumulation to the lymph nodes that could be advantageous, especially when delivering drugs that do not require transfection activity. Suggestions for future improvement to our delivery method include 1) adding an endosome escape enhancer to the S-LCP-DOPC with 20% PEGylation to boost gene expression activity, and 2) adding targeting ligands to enhance (cell-type specific) cellular uptake in the lymph nodes. If successful, S-LCP NPs could serve as a drug delivery formulation that is highly specific to the lymph nodes.

4.9 Conclusions and discussions

Based on our results, we suggest that S-LCP-DOPC with 20% PEGylation would be the most effective in achieving whole body, lymphatic drug delivery, due to highly specific accumulation in the lymph nodes after IV injection. This characteristic would be desirable in the treatment of diseases such as HIV infection. The HIV virus in the lymph

nodes is difficult to treat due to the limited ability of anti-HIV drugs to access the lymph nodes [136]. Strategies such as formulating anti-HIV drugs into lipid NPs to enhance the lymph-node-specific accumulation of anti-HIV drugs have been reported [137-140]. For instance, two CD4 targeting peptides can be used to enhance cell-type specific accumulation, by increasing the uptake of Indinavir-loaded, lipid NPs by CD4-HIV host cells [141]. However, these formulations were administered using subcutaneous injection and can only enhance the concentration of the drug in regional lymph nodes. With the lymphotropism of S-LCP-DOPC, systemic eradication of HIV infection in the lymph nodes could be possible.

If delivery to the local draining lymph nodes is all that is required, the local injection of larger particles, such as L-LCP, is sufficient. However, a majority of the NPs would most likely accumulate in the dendritic cells. This phenomenon could be advantageous for DNA vaccination since dendritic cells are one of the major antigen-presenting cells. Coating the nanoparticles with DOTAP might be preferred for the systemic, lymphatic gene delivery because it provides higher gene expression activity. Unfortunately, DOTAP has the potential to cause high gene expression in the hepatocytes, as well. As previously mentioned, S-LCP-DOPC NPs with 20% PEGylation should be able to improve the gene expression activity while preserving the high specificity to the lymph nodes by adding an endosome escape enhancer and targeting ligands.

CHAPTER V

DISCUSSIONS AND FUTURE PERSPECTIVES

5.1 Potential of S-LCP as a theranostic formulation for delivery to the lymphatic system

Efficient systemic drug delivery to the entire lymphatic organs is currently missing. As discussed in Chapter 4.1, only local drug delivery to the regional lymph nodes has been enhanced by several lipid-based NP formulations. S-LCP coated with an outer leaflet of DOPC and PEGylation showed high lymphotropsim, with more than 3 times the accumulation level (~70% ID/g) in those organs than in the liver and spleen. A comparable level of lymphotropsim has only been reported for one other particle, dextrose-coated USPIO. No other NPs have ever achieved lymph node accumulation levels similar to those of S-LCP NPs or USPIO administered by IV injection.

Several clinical studies have validated USPIO as a clinical MR imaging tool for detecting occult lymph node metastasis [100, 119, 142]. However, the ability of USPIO as a drug delivery system is very limited. No literature has reported the use of USPIO as a drug delivery system. One strategy that loaded curcumin or doxorubicin into hollow SPIO nanoshells as a theranostic delivery system has been proposed. However, this SPIO has a large particle size (hydrodynamic diameter: 191.9 ± 2.6 nm) and does not exhibit lymphotrophism [143]. Other strategies such as co-formulating USPIO with drugs using polymers [144] or block copolymers [145] also increases the size of the whole NP to above 100 nm and negates the lymphotropism of USPIO NPs.

S-LCP has been designed with drug releasing mechanisms for siRNA, chemical drugs, and cDNA (Figure 1.2). The delivery of siRNA, phosphorylated drugs (such as gemcitabine mono-phosphate), and cDNA with S-LCP has been demonstrated. This creates an opportunity for systemic lymphatic delivery of a great variety of drugs.

However, what USPIO and S-LCP-DOPC have achieved was only passive accumulation in the lymph nodes. The lymph node metastasis MR imaging of USPIO relied on passive accumulation of USPIO in the tumor-free lymph node space but not the metastatic tumor. However, because USPIO is a T2 MR imaging contrast agent that provided a dark negative signal, by comparing the MR imaging before and after administration of USPIO, the lymph node metastasis showed as a bright (positive) image. The ^{111}In loaded S-LCP-DOPC also provided a “negative imaging” of the metastasis in the lymph nodse. In order to acheive drug delivery to the metastatic tumors in the lymph nodes, the formulation might have to go one step further to reach the tumor cells.

It is possible to enhance the tumor cell-specific uptake by incorporating a tumor specific targeting ligand on S-LCP to achieve a positive delivery and imaging. If successful, this would be the first theranostic delivery system for lymph node metastasis detection and therapy.

5.2 LCP as a drug delivery system for water-insoluble drugs

In the recent past, medicinal chemists have been attempting to synthesize new chemical entities with good therapeutic effects and also acceptable water solubility. Many potent water-insoluble compounds were discarded due to lack of suitable delivery systems. Several hydrophobic drugs could be formulated in the traditional liposomal or

polymeric NPs such as the FDA approved PLGA NP formulations [146, 147]. However, the encapsulation relied on the hydrophobic interactions between the drug and the hydrophobic part of the NPs and the loading capacity was usually limited by stability issues.

The success of LCP actually provided another novel strategy to formulate water-insoluble drugs. It is possible to intentionally make water-insoluble drugs into nano-precipitates (similar to CaP) and coat them with lipid surface similar to S-LCP. If the nano-precipitates are similar in size to S-LCP NPs and the coating was successful, the new NP formulation should possess a biodistribution profile similar to that of S-LCP; the outer surface properties determine biodistribution patterns. The NPs with the drug precipitates trapped inside may exhibit a slow release that could be advantageous for cancer therapy.

5.3 LMnP as MR imaging contrast agents

The loading of ^{111}In is the first attempt to provide SPECT imaging modality to LCP NPs. Other imaging modalities such as Manganese (Mn) for MR imaging [148, 149] or Copper-64 (^{64}Cu) for PET imaging may also be formulated into LCP formulation. The feasibility of making LMnP NPs has been tested.

5.3.1 Making LMnP cores

Following the same core preparation procedure as was used for LCP, LMnP cores could be made by substituting 500 mM $CaCl_2$ with 500 mM $MnCl_2$. Using the same

Igepal surfactant system, the S-LMnP core was made to have a size comparable to S-LCP (Figure 5.1A). L-LMnP core could be made with pure Triton system. The resulting L-LMnP cores are slightly larger than L-LCP cores (Figure 5.1B). The LMnP NPs could be coated with an outer leaflet in the same manner that LCP was coated.

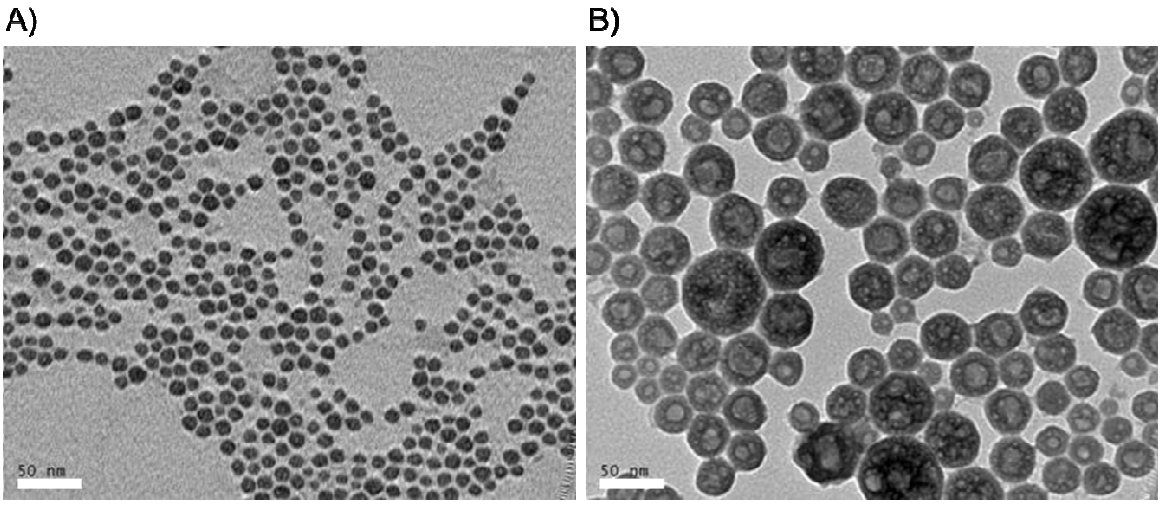

Figure 5.1 TEM images of LMnP cores

A) S-LMnP core made with the same Igepal system used for S-LCP preparation. B) L-LMnP core made with a pure Triton system. (scale bar = 50 nm)

The Mn/P ratio of the S-LMnP core has been determined to be 1.03, which is very similar to that of S-LCP (1.01 ± 0.04, Table 2.3). This suggested that MnP formed an amorphous precipitation, similar to that of CaP.

5.3.2 Preliminary demonstration of S-LMnP as MR imaging contrast agent

To test whether S-LMnP could be used as an MR imaging contrast agent, S-LMnP were coated with DOPC/cholesterol/DSPE-PEG_{2000} at 2/2/1 in a manner similar to

that of S-LCP preparation. The S-LMnP was suspended in water, put in small PCR tubes, and placed under a Bruker 9.4T horizontal bore scanner. Both T1 and T2 relaxation times were determined and compared with that of water (Figure 5.2). The effect of S-LMnP dissolution in acidic environment on its MR signal was also evaluated by adding S-LMnP in pH 4.5 and pH 2.0 buffers. The results indicated that upon dissolution, both T1 and T2 signals were enhanced. This is a preliminary experiment demonstrating the feasibility of making LMnP for MR imaging purpose.

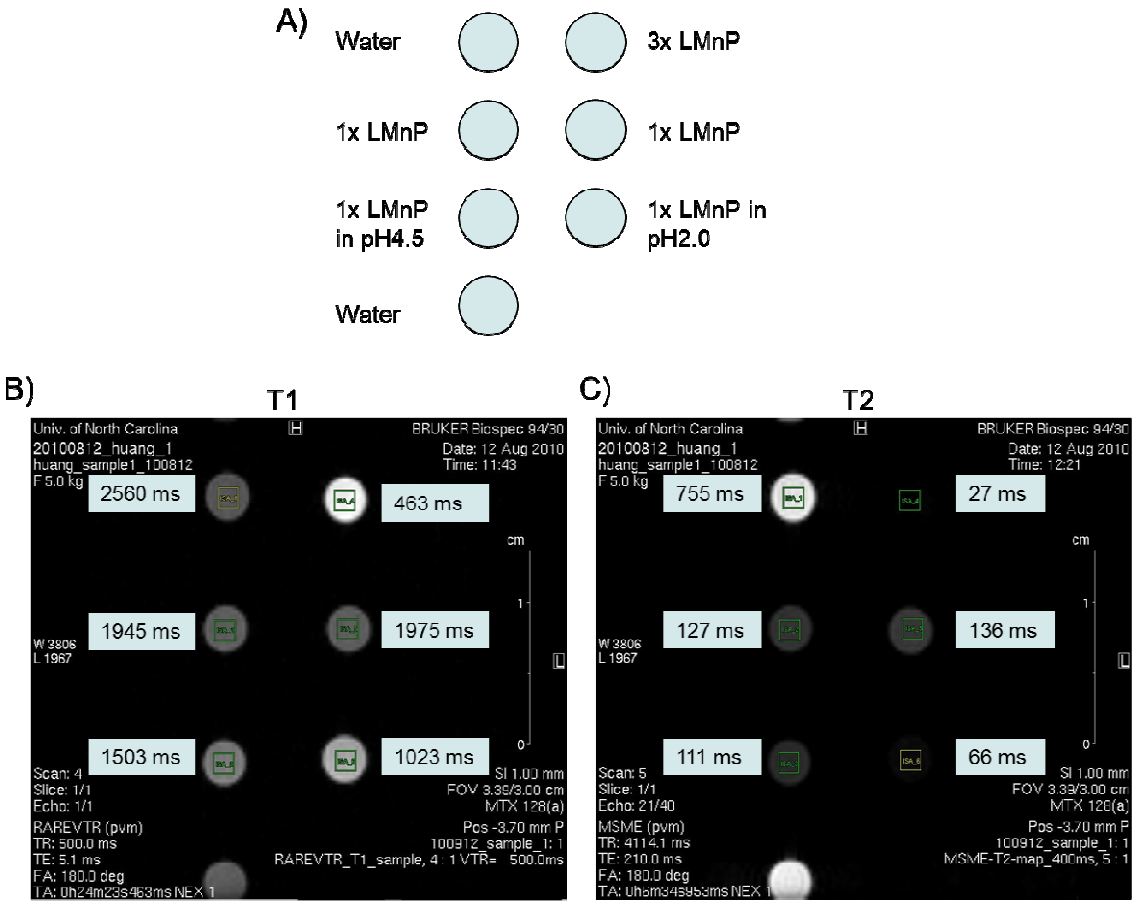

Figure 5.2 S-LMnP showed both T1 and T2 imaging capabilities

A) Sample arrangements for MR imaging. Two different concentrations of LMnP were included to show dose-dependency of T1 and T2 relaxation time-shortage. Buffers with pH 4.5 and pH 2.0 were used to mimic LMnP dissolution in acidic conditions. B) T1 imaging results. C) T2 imaging results. The T1 and T2 relaxation times of each sample were labeled accordingly.

APPENDIX

Yu-Cheng Tseng's Publication

Peer-reviewed Papers

- **Yu-Cheng Tseng** and Leaf Huang. How Does the Cell Overcome LCP Nanoparticle Induced Calcium Toxicity? (in submission)
- **Yu-Cheng Tseng**, Kevin Guley, Srinivas Ramishetti, Hong Yuan, and Leaf Huang. SPECT/CT Imaging of Tumor and Lymph Node with ^{111}In Loaded LCP Nanoparticles. (in preparation)
- **Yu-Cheng Tseng**, Zhenghong Xu, Kevin Guley, Hong Yuan, and Leaf Huang. Systemic Delivery to the Lymphatic System and SPECT/CT Imaging of Lymph Node Metastasis with LCP Nanoparticles via IV Injection. (in submission)
- Yang Liu, **Yu-Cheng Tseng**, and Leaf Huang. Biodistribution Studies of Nanoparticles Using Fluorescence Imaging: A Qualitative or Quantitative Method? Pharm Res. July, 2012
- Jun Li, Yung-Ching Chen, **Yu-Cheng Tseng**, Subho Mozumdar, and Leaf Huang. Biodegradable Calcium Phosphate Nanoparticle with Lipid Coating for Systemic siRNA Delivery. J Controlled Release 142: 416-421, 2010

Review Papers

- **Yu-Cheng Tseng** and Leaf Huang. Self-assembled Lipid Nanomedicines for siRNA Tumor Targeting. J Biomed Nanotechnol. 2009 Aug;5(4):351-63.
- **Yu-Cheng Tseng**, Subho Mozumdar, and Leaf Huang. Lipid-based Systemic Delivery of siRNA. Adv Drug Deliv Rev. 2009 Jul 25;61(9):721-31.

Conference Abstracts

- **Yu-Cheng Tseng**, Kevin Guley, Hong Yuan, and Leaf Huang. Tumor and Lymph Node SPECT/CT Imaging with In-111 Loaded LCP Nanoparticles. Gordon Research Conference on Drug Carriers in Medicine & Biology, 2012
- **Yu-Cheng Tseng**, Hong Yuan, and Leaf Huang PK Profile and Tumor Imaging with In-111 Loaded LCP Nanoparticles. Annual NCI Site Visit – Carolina CCNE, 2012
- **Yu-Cheng Tseng** and Leaf Huang. Nanoparticles Imaging Early Cellular Apoptosis. Four Annual Chapel Hill Drug Conference, Chapel Hill, NC, USA, 2009

REFERENCES

1. Ehman, R.L., et al., *Blueprint for imaging in biomedical research.* Radiology, 2007. **244**(1): p. 12-27.

2. Hillman, B.J., *Introduction to the special issue on medical imaging in oncology.* J Clin Oncol, 2006. **24**(20): p. 3223-4.

3. Atri, M., *New technologies and directed agents for applications of cancer imaging.* J Clin Oncol, 2006. **24**(20): p. 3299-308.

4. Kent, M.S., J.L. Port, and N.K. Altorki, *Current state of imaging for lung cancer staging.* Thorac Surg Clin, 2004. **14**(1): p. 1-13.

5. Lee, K.S., et al., *T1 non-small cell lung cancer: imaging and histopathologic findings and their prognostic implications.* Radiographics, 2004. **24**(6): p. 1617-36; discussion 1632-6.

6. Ferme, C., et al., *Role of imaging to choose treatment.* Cancer Imaging, 2005. **5 Spec No A**: p. S113-9.

7. Singhal, S., S. Nie, and M.D. Wang, *Nanotechnology applications in surgical oncology.* Annu Rev Med, 2010. **61**: p. 359-73.

8. Mohs, A.M., et al., *Hand-held Spectroscopic Device for In Vivo and Intraoperative Tumor Detection: Contrast Enhancement, Detection Sensitivity, and Tissue Penetration.* Anal Chem, 2010.

9. Brindle, K., *New approaches for imaging tumour responses to treatment.* Nat Rev Cancer, 2008. **8**(2): p. 94-107.

10. Keidar, Z., et al., *PET/CT using 18F-FDG in suspected lung cancer recurrence: diagnostic value and impact on patient management.* J Nucl Med, 2004. **45**(10): p. 1640-6.

11. Fass, L., *Imaging and cancer: a review.* Mol Oncol, 2008. **2**(2): p. 115-52.

12. Hong, G., et al., *Multifunctional in vivo vascular imaging using near-infrared II fluorescence.* Nat Med, 2012.

13. Kim, S., et al., *Near-infrared fluorescent type II quantum dots for sentinel lymph node mapping.* Nat Biotechnol, 2004. **22**(1): p. 93-7.

14. Hong, G., et al., *Near-infrared-fluorescence-enhanced molecular imaging of live cells on gold substrates.* Angew Chem Int Ed Engl, 2011. **50**(20): p. 4644-8.

15. Hong, G., et al., *Three-dimensional imaging of single nanotube molecule endocytosis on plasmonic substrates.* Nat Commun, 2012. **3**: p. 700.

16. Smith, A.M., M.C. Mancini, and S. Nie, *Bioimaging: second window for in vivo imaging.* Nat Nanotechnol, 2009. **4**(11): p. 710-1.

17. Perry, S.W., R.M. Burke, and E.B. Brown, *Two-photon and second harmonic microscopy in clinical and translational cancer research.* Ann Biomed Eng, 2012. **40**(2): p. 277-91.

18. Provenzano, P.P., K.W. Eliceiri, and P.J. Keely, *Multiphoton microscopy and fluorescence lifetime imaging microscopy (FLIM) to monitor metastasis and the tumor microenvironment.* Clin Exp Metastasis, 2009. **26**(4): p. 357-70.

19. Qian, X., et al., *In vivo tumor targeting and spectroscopic detection with surface-enhanced Raman nanoparticle tags.* Nat Biotechnol, 2008. **26**(1): p. 83-90.

20. Qian, X., J. Li, and S. Nie, *Stimuli-responsive SERS nanoparticles: conformational control of plasmonic coupling and surface Raman enhancement.* J Am Chem Soc, 2009. **131**(22): p. 7540-1.

21. Nie, S. and S.R. Emory, *Probing Single Molecules and Single Nanoparticles by Surface-Enhanced Raman Scattering.* Science, 1997. **275**(5303): p. 1102-6.

22. Psimadas, D., et al., *Molecular nanomedicine towards cancer: (111) In-labeled nanoparticles.* J Pharm Sci, 2012. **101**(7): p. 2271-80.

23. Kelkar, S.S. and T.M. Reineke, *Theranostics: combining imaging and therapy.* Bioconjug Chem, 2011. **22**(10): p. 1879-903.

24. Doane, T.L. and C. Burda, *The unique role of nanoparticles in nanomedicine: imaging, drug delivery and therapy.* Chem Soc Rev, 2012. **41**(7): p. 2885-911.

25. Nam, J., et al., *Surface engineering of inorganic nanoparticles for imaging and therapy.* Adv Drug Deliv Rev, 2012.

26. Liu, Y. and M.J. Welch, *Nanoparticles labeled with positron emitting nuclides: advantages, methods, and applications.* Bioconjug Chem, 2012. **23**(4): p. 671-82.

27. Keidar, Z., O. Israel, and Y. Krausz, *SPECT/CT in tumor imaging: technical aspects and clinical applications.* Semin Nucl Med, 2003. **33**(3): p. 205-18.

28. Kim, W., et al., *Use of lymphoscintigraphy with SPECT/CT for sentinel node localization in a case of vaginal melanoma.* Clin Nucl Med, 2006. **31**(4): p. 201-2.

29. Ishihara, T., et al., *Management of sentinel lymph nodes in malignant skin tumors using dynamic lymphoscintigraphy and the single-photon-emission computed tomography/computed tomography combined system.* Int J Clin Oncol, 2006. **11**(3): p. 214-20.

30. Khafif, A., et al., *Lymphoscintigraphy for sentinel node mapping using a hybrid single photon emission CT (SPECT)/CT system in oral cavity squamous cell carcinoma.* Head Neck, 2006. **28**(10): p. 874-9.

31. Even-Sapir, E., et al., *Lymphoscintigraphy for sentinel node mapping using a hybrid SPECT/CT system.* J Nucl Med, 2003. **44**(9): p. 1413-20.

32. Kizu, H., et al., *Fusion of SPECT and multidetector CT images for accurate localization of pelvic sentinel lymph nodes in prostate cancer patients.* J Nucl Med Technol, 2005. **33**(2): p. 78-82.

33. Sherif, A., et al., *Hybrid SPECT-CT: an additional technique for sentinel node detection of patients with invasive bladder cancer.* Eur Urol, 2006. **50**(1): p. 83-91.

34. Hicks, R., E. Lau, and D. Binns, *Hybrid imaging is the future of molecular imaging.* Biomed Imaging Interv J, 2007. **3**(3): p. e49.

35. Sanvicens, N. and M.P. Marco, *Multifunctional nanoparticles--properties and prospects for their use in human medicine.* Trends Biotechnol, 2008. **26**(8): p. 425-33.

36. Li, S.D. and L. Huang, *Targeted delivery of antisense oligodeoxynucleotide and small interference RNA into lung cancer cells.* Mol Pharm, 2006. **3**(5): p. 579-88.

37. Li, S.D., et al., *Tumor-targeted delivery of siRNA by self-assembled nanoparticles.* Mol Ther, 2008. **16**(1): p. 163-9.

38. Li, S.D., S. Chono, and L. Huang, *Efficient gene silencing in metastatic tumor by siRNA formulated in surface-modified nanoparticles.* J Control Release, 2008. **126**(1): p. 77-84.

39. Li, S.D., S. Chono, and L. Huang, *Efficient oncogene silencing and metastasis inhibition via systemic delivery of siRNA.* Mol Ther, 2008. **16**(5): p. 942-6.

40. Li, J., Y. Yang, and L. Huang, *Calcium phosphate nanoparticles with an asymmetric lipid bilayer coating for siRNA delivery to the tumor.* J Control Release, 2012. **158**(1): p. 108-14.

41. Yang, Y., et al., *Nanoparticle Delivery of Pooled siRNA for Effective Treatment of Non-Small Cell Lung Caner.* Mol Pharm, 2012.

42. Yang, Y., et al., *Systemic delivery of siRNA via LCP nanoparticle efficiently inhibits lung metastasis.* Mol Ther, 2012. **20**(3): p. 609-15.

43. Liu, Z., et al., *In vivo biodistribution and highly efficient tumour targeting of carbon nanotubes in mice.* Nat Nanotechnol, 2007. **2**(1): p. 47-52.

44. Villa, C.H., et al., *Synthesis and biodistribution of oligonucleotide-functionalized, tumor-targetable carbon nanotubes.* Nano Lett, 2008. **8**(12): p. 4221-8.

45. Rojas, S., et al., *Biodistribution of amino-functionalized diamond nanoparticles. In vivo studies based on 18F radionuclide emission.* ACS Nano, 2011. **5**(7): p. 5552-9.

46. Maeda, H., *Macromolecular therapeutics in cancer treatment: The EPR effect and beyond.* J Control Release, 2012.

47. Maeda, H., H. Nakamura, and J. Fang, *The EPR effect for macromolecular drug delivery to solid tumors: Improvement of tumor uptake, lowering of systemic toxicity, and distinct tumor imaging in vivo.* Adv Drug Deliv Rev, 2012.

48. Hong, S., et al., *The binding avidity of a nanoparticle-based multivalent targeted drug delivery platform.* Chem Biol, 2007. **14**(1): p. 107-15.

49. Debbage, P. and W. Jaschke, *Molecular imaging with nanoparticles: giant roles for dwarf actors.* Histochem Cell Biol, 2008. **130**(5): p. 845-75.

50. Popielarski, S.R., et al., *A nanoparticle-based model delivery system to guide the rational design of gene delivery to the liver. 2. In vitro and in vivo uptake results.* Bioconjug Chem, 2005. **16**(5): p. 1071-80.

51. Tseng, Y.C., S. Mozumdar, and L. Huang, *Lipid-based systemic delivery of siRNA.* Adv Drug Deliv Rev, 2009. **61**(9): p. 721-31.

52. Maruyama, K., S.J. Kennel, and L. Huang, *Lipid composition is important for highly efficient target binding and retention of immunoliposomes.* Proc Natl Acad Sci U S A, 1990. **87**(15): p. 5744-8.

53. Zhang, G., et al., *Influence of anchoring ligands and particle size on the colloidal stability and in vivo biodistribution of polyethylene glycol-coated gold nanoparticles in tumor-xenografted mice.* Biomaterials, 2009. **30**(10): p. 1928-36.

54. Verbaan, F.J., et al., *Steric stabilization of poly(2-(dimethylamino)ethyl methacrylate)-based polyplexes mediates prolonged circulation and tumor targeting in mice.* J Gene Med, 2004. **6**(1): p. 64-75.

55. Woodle, M.C., *Surface-modified liposomes: assessment and characterization for increased stability and prolonged blood circulation.* Chem Phys Lipids, 1993. **64**(1-3): p. 249-62.

56. Folkman, J., *Angiogenesis: an organizing principle for drug discovery?* Nat Rev Drug Discov, 2007. **6**(4): p. 273-86.

57. Matsumura, Y. and H. Maeda, *A new concept for macromolecular therapeutics in cancer chemotherapy: mechanism of tumoritropic accumulation of proteins and the antitumor agent smancs.* Cancer Res, 1986. **46**(12 Pt 1): p. 6387-92.

58. Park, J.W., *Liposome-based drug delivery in breast cancer treatment.* Breast Cancer Res, 2002. **4**(3): p. 95-9.

59. Allen, T.M. and P.R. Cullis, *Drug delivery systems: entering the mainstream.* Science, 2004. **303**(5665): p. 1818-22.

60. Greish, K., *Enhanced permeability and retention (EPR) effect for anticancer nanomedicine drug targeting.* Methods Mol Biol, 2010. **624**: p. 25-37.

61. Konno, T., et al., *Effect of arterial administration of high-molecular-weight anticancer agent SMANCS with lipid lymphographic agent on hepatoma: a*

preliminary report. Eur J Cancer Clin Oncol, 1983. **19**(8): p. 1053-65.

62. Konno, T., et al., *Selective targeting of anti-cancer drug and simultaneous image enhancement in solid tumors by arterially administered lipid contrast medium.* Cancer, 1984. **54**(11): p. 2367-74.

63. Maki, S., T. Konno, and H. Maeda, *Image enhancement in computerized tomography for sensitive diagnosis of liver cancer and semiquantitation of tumor selective drug targeting with oily contrast medium.* Cancer, 1985. **56**(4): p. 751-7.

64. Nagayasu, A., K. Uchiyama, and H. Kiwada, *The size of liposomes: a factor which affects their targeting efficiency to tumors and therapeutic activity of liposomal antitumor drugs.* Adv Drug Deliv Rev, 1999. **40**(1-2): p. 75-87.

65. Tang, L., et al., *Synthesis and biological response of size-specific, monodisperse drug-silica nanoconjugates.* ACS Nano, 2012. **6**(5): p. 3954-66.

66. Zamboni, W.C., et al., *Systemic and tumor disposition of platinum after administration of cisplatin or STEALTH liposomal-cisplatin formulations (SPI-077 and SPI-077 B103) in a preclinical tumor model of melanoma.* Cancer Chemother Pharmacol, 2004. **53**(4): p. 329-36.

67. Yamada, A., et al., *Design of folate-linked liposomal doxorubicin to its antitumor effect in mice.* Clin Cancer Res, 2008. **14**(24): p. 8161-8.

68. Low, P.S., W.A. Henne, and D.D. Doorneweerd, *Discovery and development of folic-acid-based receptor targeting for imaging and therapy of cancer and inflammatory diseases.* Acc Chem Res, 2008. **41**(1): p. 120-9.

69. Reddy, J.A., V.M. Allagadda, and C.P. Leamon, *Targeting therapeutic and imaging agents to folate receptor positive tumors.* Curr Pharm Biotechnol, 2005. **6**(2): p. 131-50.

70. Hilgenbrink, A.R. and P.S. Low, *Folate receptor-mediated drug targeting: from therapeutics to diagnostics.* J Pharm Sci, 2005. **94**(10): p. 2135-46.

71. Banerjee, R., et al., *Anisamide-targeted stealth liposomes: a potent carrier for targeting doxorubicin to human prostate cancer cells.* Int J Cancer, 2004. **112**(4): p. 693-700.

72. John, C.S., et al., *Targeting sigma receptor-binding benzamides as in vivo diagnostic and therapeutic agents for human prostate tumors.* Cancer Res, 1999. **59**(18): p. 4578-83.

73. Mukherjee, A., et al., *Haloperidol-associated stealth liposomes: a potent carrier for delivering genes to human breast cancer cells.* J Biol Chem, 2005. **280**(16): p. 15619-27.

74. Vilner, B.J., C.S. John, and W.D. Bowen, *Sigma-1 and sigma-2 receptors are expressed in a wide variety of human and rodent tumor cell lines.* Cancer Res, 1995. **55**(2): p. 408-13.

75. John, C.S., et al., *A malignant melanoma imaging agent: synthesis, characterization, in vitro binding and biodistribution of iodine-125-(2-piperidinylaminoethyl)4-iodobenzamide.* J Nucl Med, 1993. **34**(12): p. 2169-75.

76. John, C.S., et al., *Synthesis and pharmacological characterization of 4-[125I]-N-(N-benzylpiperidin-4-yl)-4-iodobenzamide: a high affinity sigma receptor ligand for potential imaging of breast cancer.* Cancer Res, 1995. **55**(14): p. 3022-7.

77. Meares, C.F., et al., *Macrocyclic chelates of radiometals for diagnosis and therapy.* Br J Cancer Suppl, 1990. **10**: p. 21-6.

78. Wang, Y., et al., *Evaluating the pharmacokinetics and in vivo cancer targeting capability of au nanocages by positron emission tomography imaging.* ACS Nano, 2012. **6**(7): p. 5880-8.

79. Li, S.D. and L. Huang, *Nanoparticles evading the reticuloendothelial system: role of the supported bilayer.* Biochim Biophys Acta, 2009. **1788**(10): p. 2259-66.

80. Kingston, R.E., C.A. Chen, and J.K. Rose, *Calcium phosphate transfection.* Curr Protoc Mol Biol, 2003. **Chapter 9**: p. Unit 9 1.

81. Li, J., et al., *Biodegradable calcium phosphate nanoparticle with lipid coating for systemic siRNA delivery.* J Control Release, 2010. **142**(3): p. 416-21.

82. Vaccaro, J.A., et al., *Mechanism of inhibition of the human immunodeficiency virus type 1 reverse transcriptase by d4TTP: an equivalent incorporation efficiency relative to the natural substrate dTTP.* Antimicrob Agents Chemother, 2000. **44**(1): p. 217-21.

83. Ray, A.S., et al., *Insights into the molecular mechanism of inhibition and drug resistance for HIV-1 RT with carbovir triphosphate.* Biochemistry, 2002. **41**(16): p. 5150-62.

84. Menendez-Arias, L., *Mechanisms of resistance to nucleoside analogue inhibitors of HIV-1 reverse transcriptase.* Virus Res, 2008. **134**(1-2): p. 124-46.

85. Painter, G.R., et al., *Biochemical and mechanistic basis for the activity of nucleoside analogue inhibitors of HIV reverse transcriptase.* Curr Top Med Chem, 2004. **4**(10): p. 1035-44.

86. Dong, H., et al., *Long-circulating 15 nm micelles based on amphiphilic 3-helix peptide-PEG conjugates.* ACS Nano, 2012. **6**(6): p. 5320-9.

87. Almeida, J.P., et al., *In vivo biodistribution of nanoparticles.* Nanomedicine (Lond), 2011. **6**(5): p. 815-35.

88. Graham, M.J., et al., *Tritium labeling of antisense oligonucleotides by exchange with tritiated water.* Nucleic Acids Res, 1993. **21**(16): p. 3737-43.

89. Zong, W.X. and C.B. Thompson, *Necrotic death as a cell fate.* Genes Dev, 2006. **20**(1): p. 1-15.

90. Vanlangenakker, N., et al., *Molecular mechanisms and pathophysiology of necrotic cell death.* Curr Mol Med, 2008. **8**(3): p. 207-20.

91. Wrogemann, K. and S.D. Pena, *Mitochondrial calcium overload: A general mechanism for cell-necrosis in muscle diseases.* Lancet, 1976. **1**(7961): p. 672-4.

92. Landon, E.J., R.J. Naukam, and B.V. Rama Sastry, *Effects of calcium channel blocking agents on calcium and centrilobular necrosis in the liver of rats treated with hepatotoxic agents.* Biochem Pharmacol, 1986. **35**(4): p. 697-705.

93. McConkey, D.J. and S. Orrenius, *The role of calcium in the regulation of apoptosis.* J Leukoc Biol, 1996. **59**(6): p. 775-83.

94. Nicholls, D.G., *Intracellular calcium homeostasis.* Br Med Bull, 1986. **42**(4): p. 353-8.

95. Chaudhary, J., et al., *Caloxin: a novel plasma membrane Ca2+ pump inhibitor.* Am J Physiol Cell Physiol, 2001. **280**(4): p. C1027-30.

96. Szewczyk, M.M., J. Pande, and A.K. Grover, *Caloxins: a novel class of selective plasma membrane Ca2+ pump inhibitors obtained using biotechnology.* Pflugers Arch, 2008. **456**(2): p. 255-66.

97. Holmes, M.E., J. Chaudhary, and A.K. Grover, *Mechanism of action of the novel plasma membrane Ca(2+)-pump inhibitor caloxin.* Cell Calcium, 2003. **33**(4): p. 241-5.

98. Garcia-Rivas Gde, J., et al., *Ru360, a specific mitochondrial calcium uptake inhibitor, improves cardiac post-ischaemic functional recovery in rats in vivo.* Br J Pharmacol, 2006. **149**(7): p. 829-37.

99. Griffiths, E.J., *Mitochondrial calcium transport in the heart: physiological and pathological roles.* J Mol Cell Cardiol, 2009. **46**(6): p. 789-803.

100. Harisinghani, M.G., et al., *Noninvasive detection of clinically occult lymph-node metastases in prostate cancer.* N Engl J Med, 2003. **348**(25): p. 2491-9.

101. Rockall, A.G., et al., *Diagnostic performance of nanoparticle-enhanced magnetic resonance imaging in the diagnosis of lymph node metastases in patients with endometrial and cervical cancer.* J Clin Oncol, 2005. **23**(12): p. 2813-21.

102. Nakai, G., et al., *Evaluation of axillary lymph nodes by diffusion-weighted MRI using ultrasmall superparamagnetic iron oxide in patients with breast cancer: initial clinical experience.* J Magn Reson Imaging, 2011. **34**(3): p. 557-62.

103. Triantafyllou, M., et al., *Ultrasmall superparamagnetic particles of iron oxide allow for the detection of metastases in normal sized pelvic lymph nodes of patients with bladder and/or prostate cancer.* Eur J Cancer, 2012.

104. Harisinghani, M.G., et al., *Ferumoxtran-10-enhanced MR lymphangiography: does contrast-enhanced imaging alone suffice for accurate lymph node*

characterization? AJR Am J Roentgenol, 2006. **186**(1): p. 144-8.

105. Liu, Y., Y.C. Tseng, and L. Huang, *Biodistribution studies of nanoparticles using fluorescence imaging: a qualitative or quantitative method?* Pharm Res, 2012. **29**(12): p. 3273-7.

106. Hak, S., et al., *The effect of nanoparticle polyethylene glycol surface density on ligand-directed tumor targeting studied in vivo by dual modality imaging.* ACS Nano, 2012. **6**(6): p. 5648-58.

107. Kirpotin, D.B., et al., *Antibody targeting of long-circulating lipidic nanoparticles does not increase tumor localization but does increase internalization in animal models.* Cancer Res, 2006. **66**(13): p. 6732-40.

108. Bartlett, D.W., et al., *Impact of tumor-specific targeting on the biodistribution and efficacy of siRNA nanoparticles measured by multimodality in vivo imaging.* Proc Natl Acad Sci U S A, 2007. **104**(39): p. 15549-54.

109. Doi, Y., et al., *Combination therapy of metronomic S-1 dosing with oxaliplatin-containing polyethylene glycol-coated liposome improves antitumor activity in a murine colorectal tumor model.* Cancer Sci, 2010. **101**(11): p. 2470-5.

110. Maeda, H., *Nitroglycerin enhances vascular blood flow and drug delivery in hypoxic tumor tissues: analogy between angina pectoris and solid tumors and enhancement of the EPR effect.* J Control Release, 2010. **142**(3): p. 296-8.

111. Hawkins, B.T. and R.D. Egleton, *Fluorescence imaging of blood-brain barrier disruption.* J Neurosci Methods, 2006. **151**(2): p. 262-7.

112. Xanthos, D.N., et al., *Effects of peripheral inflammation on the blood-spinal cord barrier.* Mol Pain, 2012. **8**: p. 44.

113. Politi, K. and W. Pao, *How genetically engineered mouse tumor models provide insights into human cancers.* J Clin Oncol, 2011. **29**(16): p. 2273-81.

114. Xiong, S., J. Parker-Thornburg, and G. Lozano, *Developing genetically engineered mouse models to study tumor suppression.* Curr Protoc Mouse Biol, 2012. **2**(1): p. 9-24.

115. Tentler, J.J., et al., *Patient-derived tumour xenografts as models for oncology drug development.* Nat Rev Clin Oncol, 2012. **9**(6): p. 338-50.

116. Tammela, T. and K. Alitalo, *Lymphangiogenesis: Molecular mechanisms and future promise.* Cell, 2010. **140**(4): p. 460-76.

117. Huang, X., et al., *Long-term multimodal imaging of tumor draining sentinel lymph nodes using mesoporous silica-based nanoprobes.* Biomaterials, 2012. **33**(17): p. 4370-8.

118. Kamala, T., *Hock immunization: a humane alternative to mouse footpad injections.* J Immunol Methods, 2007. **328**(1-2): p. 204-14.

119. Zhang, F., et al., *Differentiation of Reactive and Tumor Metastatic Lymph Nodes with Diffusion-weighted and SPIO-Enhanced MRI.* Mol Imaging Biol, 2012.

120. Xie, Y., et al., *Drug delivery to the lymphatic system: importance in future cancer diagnosis and therapies.* Expert Opin Drug Deliv, 2009. **6**(8): p. 785-92.

121. Chambers, A.F., A.C. Groom, and I.C. MacDonald, *Dissemination and growth of cancer cells in metastatic sites.* Nat Rev Cancer, 2002. **2**(8): p. 563-72.

122. Pantel, K. and R.H. Brakenhoff, *Dissecting the metastatic cascade.* Nat Rev Cancer, 2004. **4**(6): p. 448-56.

123. Sleeman, J.P., *The relationship between tumors and the lymphatics: what more is there to know?* Lymphology, 2006. **39**(2): p. 62-8.

124. Porter, C.J., *Drug delivery to the lymphatic system.* Crit Rev Ther Drug Carrier Syst, 1997. **14**(4): p. 333-93.

125. Reddy, L.H. and R.S. Murthy, *Pharmacokinetics and biodistribution studies of Doxorubicin loaded poly(butyl cyanoacrylate) nanoparticles synthesized by two different techniques.* Biomed Pap Med Fac Univ Palacky Olomouc Czech Repub, 2004. **148**(2): p. 161-6.

126. Kaminskas, L.M. and C.J. Porter, *Targeting the lymphatics using dendritic polymers (dendrimers).* Adv Drug Deliv Rev, 2011. **63**(10-11): p. 890-900.

127. Cai, S., et al., *Lymphatic drug delivery using engineered liposomes and solid lipid nanoparticles.* Adv Drug Deliv Rev, 2011. **63**(10-11): p. 901-8.

128. Erogbogbo, F., et al., *In vivo targeted cancer imaging, sentinel lymph node mapping and multi-channel imaging with biocompatible silicon nanocrystals.* ACS Nano, 2011. **5**(1): p. 413-23.

129. Tang, L., et al., *Aptamer-Functionalized, Ultra-Small, Monodisperse Silica Nanoconjugates for Targeted Dual-Modal Imaging of Lymph Nodes with Metastatic Tumors.* Angew Chem Int Ed Engl, 2012.

130. Lievens, J., et al., *The size of sinusoidal fenestrae is a critical determinant of hepatocyte transduction after adenoviral gene transfer.* Gene Ther, 2004. **11**(20): p. 1523-31.

131. Mou, Y., et al., *In vivo migration of dendritic cells labeled with synthetic superparamagnetic iron oxide.* Int J Nanomedicine, 2011. **6**: p. 2633-40.

132. Arvizo, R.R., et al., *Modulating pharmacokinetics, tumor uptake and biodistribution by engineered nanoparticles.* PLoS One, 2011. **6**(9): p. e24374.

133. Harivardhan Reddy, L., et al., *Influence of administration route on tumor uptake and biodistribution of etoposide loaded solid lipid nanoparticles in Dalton's lymphoma tumor bearing mice.* J Control Release, 2005. **105**(3): p. 185-98.

134. Romberg, B., W.E. Hennink, and G. Storm, *Sheddable coatings for long-circulating nanoparticles.* Pharm Res, 2008. **25**(1): p. 55-71.

135. Li, S.D. and L. Huang, *Stealth nanoparticles: high density but sheddable PEG is a key for tumor targeting.* J Control Release, 2010. **145**(3): p. 178-81.

136. Cavert, W., et al., *Kinetics of response in lymphoid tissues to antiretroviral therapy of HIV-1 infection.* Science, 1997. **276**(5314): p. 960-4.

137. Desormeaux, A. and M.G. Bergeron, *Lymphoid tissue targeting of anti-HIV drugs using liposomes.* Methods Enzymol, 2005. **391**: p. 330-51.

138. Kinman, L., et al., *Lipid-drug association enhanced HIV-1 protease inhibitor indinavir localization in lymphoid tissues and viral load reduction: a proof of concept study in HIV-2287-infected macaques.* J Acquir Immune Defic Syndr, 2003. **34**(4): p. 387-97.

139. Gagne, J.F., et al., *Targeted delivery of indinavir to HIV-1 primary reservoirs with immunoliposomes.* Biochim Biophys Acta, 2002. **1558**(2): p. 198-210.

140. Kinman, L., et al., *Optimization of lipid-indinavir complexes for localization in lymphoid tissues of HIV-infected macaques.* J Acquir Immune Defic Syndr, 2006. **42**(2): p. 155-61.

141. Endsley, A.N. and R.J. Ho, *Enhanced anti-HIV efficacy of Indinavir after inclusion in CD4 targeted lipid nanoparticles.* J Acquir Immune Defic Syndr, 2012.

142. Mouli, S.K., et al., *Lymphotropic nanoparticle enhanced MRI for the staging of genitourinary tumors.* Nat Rev Urol, 2010. **7**(2): p. 84-93.

143. Zhu, X.M., et al., *Hollow superparamagnetic iron oxide nanoshells as a hydrophobic anticancer drug carrier: intracelluar pH-dependent drug release and enhanced cytotoxicity.* Nanoscale, 2012. **4**(18): p. 5744-54.

144. Ling, Y., et al., *Dual docetaxel/superparamagnetic iron oxide loaded nanoparticles for both targeting magnetic resonance imaging and cancer therapy.* Biomaterials, 2011. **32**(29): p. 7139-50.

145. Hu, J., et al., *Drug-loaded and superparamagnetic iron oxide nanoparticle surface-embedded amphiphilic block copolymer micelles for integrated chemotherapeutic drug delivery and MR imaging.* Langmuir, 2012. **28**(4): p. 2073-82.

146. Fonseca, C., S. Simoes, and R. Gaspar, *Paclitaxel-loaded PLGA nanoparticles: preparation, physicochemical characterization and in vitro anti-tumoral activity.* J Control Release, 2002. **83**(2): p. 273-286.

147. Danhier, F., et al., *PLGA-based nanoparticles: an overview of biomedical applications.* J Control Release, 2012. **161**(2): p. 505-22.

148. Shapiro, E.M. and A.P. Koretsky, *Convertible manganese contrast for molecular*

and cellular MRI. Magn Reson Med, 2008. **60**(2): p. 265-9.

149. Aoki, I., et al., *Cell labeling for magnetic resonance imaging with the T1 agent manganese chloride.* NMR Biomed, 2006. **19**(1): p. 50-9.